Mesoscopic Photonic Crystal Devices

Department of Electrical and Information Engineering
ELECTRICAL AND INFORMATION ENGINEERING
Ph.D. Program
SSD: ING-INF/02–ELECTROMAGNETIC FIELDS

**Final Dissertation**

---

# Mesoscopic Photonic Crystal Devices

---

by
Ferrara Benedetta

Supervisor:

Prof. Antonella D'Orazio

Co-Supervisor:

Dott. Marco Grande

*Coordinator of Ph.D. Program:*
*Prof. Alfredo Grieco*

---

*Course n°31, 01/11/2015-31/10/2018*

Politecnico di Bari

Department of Electrical and Information Engineering
ELECTRICAL AND INFORMATION ENGINEERING
Ph.D. Program
SSD: ING-INF/02–ELECTROMAGNETIC FIELDS

**Final Dissertation**

# Mesoscopic Photonic Crystal Devices

by

Ferrara Benedetta :

Benedetta Ferrara

Referees:

Prof. Salah Obayya

Dr. Abdul Shakoor

Supervisor:

Prof. Antonella D'Orazio

Antonella D'Orazio

Co-Supervisor:

Dott. Marco Grande

*Coordinator of Ph.D Program:*

*Prof. Alfredo Grieco*

*Course n°31, 01/11/2015-31/10/2018*

**CONTENTS**

**Introduction……..1**

**1. Mesoscopic Photonic Crystals……..3**

**1.1 Mesoscopic Photonic Crystals State of Art……3**

**1.2 Mesoscopic Photonic Crystals Applications……...6**

**1.2.1 Refractive index sensor……6**

**1.2.2 Optical trapping in air and in water……...7**

**1.3 Mesoscopic self-collimation principle…….....9**

**1.3.1 Propagation inside an isotropic or anisotropic medium……...9**

**1.3.2 The index of curvature……...10**

**1.3.3 Propagation through a bulk medium/PhC interface……..10**

**1.3.4 Mesoscopic Self-Collimation condition……13**

**1.4 The 2D and 3D designs of the geometries of the single MPhC multilayers...15**

**1.4.1 Properties of the 2D and 3D unitary cells of PhCs …….15**

**1.4.2 Tailored overall reflectivity……...19**

**1.4.2.1 Single AR and HR MPhC multilayers searching algorithm……20**

**2. Mesoscopic Photonic Crystal cavities……..25**

**2.1 Mesoscopic Photonic Crystal 2D strip cavity devoted to refractive index sensor……...25**

**2.2 Mesoscopic Photonic Crystal 3D strip cavity devoted to refractive index sensor……...29**

**2.3 The experimental demonstration of Mesoscopic Photonic Crystal 3D strip cavity ……...……32**

**2.4 Mesoscopic Photonic Crystal 3D wide cavity devoted to optical trapping in air……..39**

**2.5 Mesoscopic Photonic Crystal 3D wide cavity devoted to optical trapping in water……47**

**3. Mesoscopic Photonic Crystal waveguides……54**

**3.1 Mesoscopic Photonic Crystal 3D strip and 3D wide waveguides devoted to routing element……..54**

**3.2 Mesoscopic Photonic Crystal 3D wide waveguide: the influence of the gaussian source waist on the collimation phenomenon……..58**

**3.3 Mesoscopic Photonic Crystal 3D wide waveguide with tilted source devoted to obtain Mesoscopic Self-Collimation along tilted direction……62**

**4. Conclusion……..65**

**Bibliografy……..68**

# INTRODUCTION

This Ph.D. thesis focuses on the design and the analysis of high performance Mesoscopic Photonic Crystal (MPhC) 3D waveguides and cavities. Moreover, in this thesis it has been numerically demonstrated the efficiency of these 3D MPhC devices for applications as refractive index sensors, optical trapping in air or in water, and routing element. This thesis is based on a collaboration among Politecnico di Bari, C2N CNRS of Université Paris-Sud and LAAS-CNRS of Toulouse.

In the Chapter 1 ("Mesoscopic Photonic Crystals"), the MPhCs State of Art (Paragraph 1.1), the MPhCs Applications (Paragraph 1.2), the MSC principle (Paragraph 1.3) and the 2D and 3D designs of the geometries of the single MPhC multilayers (Paragraph 1.4) have been illustrated.

In the "MPhCs State of Art" (Paragraph 1.1), a review of Self-Collimation (SC) phenomenon in traditional Photonic Crystals (PhCs), in metamaterials, in sonic crystals and plasmonic crystals in recent literature has been presented. This paragraph has highlighted the wide interest devoted to SC inside PhC, the SC problems and limitations, and has illustrated that MPhC 2D devices based on MSC are an alternative of the traditional PhCs since they avoid SC limitations. Aim of this paragraph is also to highlight the performance variations of the MPhC 2D and 3D structures. The analysis of 3D structures is very complex and onerous from the point of view of required memory and calculation time, but it is necessary when we want to carry out a realistic design of structures for sensoring, optical trapping and routing element.

In the "MPhCs Applications" (Paragraph 1.2), a review of refractive index sensors and optical trapping in air and in water in recent literature has been presented.

The Paragraph 1.2.1 ("Refractive index sensor") has highlighted the wide interest devoted to refractive index sensors based on ring resonators, microstructured optical fibers, plasmonic crystals and PhCs. Aim of this paragraph is to highlight that MPhC 2D and 3D strip microcavities can be exploited to tweeze-and-sense micro- and nano-object systems thanks to the translation invariance property.

The Paragraph 1.2.2 (“Optical trapping in air and in water”) has highlighted the wide interest devoted to optoelectronic-, plasmonic-, solid core waveguide-, PhC-based tweezers for optical trapping and manipulation (OTM) for biological applications in liquid environments, and the wide interest devoted to OTM of air particulate. Aim of this paragraph is to discuss the possibility to design a high performance MPhC 3D wide microcavity for optical trapping of fine particulate matter in air. This device may be suitable to linearly reposition nano- and micro-particles exploiting the translational invariance. The MPhC 3D wide microcavity can be exploited for optical bio-trapping in water.

In the “MSC principle” Paragraph 1.3, after an introduction on the essential tools for dealing with MSC, the condition ensuring this phenomenon has been detailed. The considered MPhC mesoperiod is obtained by interleaving focusing slab, constituted by hole rows of a 45°-tilted hole-type square-lattice PhC, and defocusing slab, constituted by bulk material, etched on a membrane.

In Paragraph 1.4 some results regarding the 2D and 3D design of MPhC multilayers of the 3D cavities and waveguides are illustrated.

Chapter 2 (“Mesoscopic Photonic Crystal cavities”) reports some results regarding the MPhC 2D and 3D strip cavities devoted to refractive index sensor (Paragraph 2.1 and Paragraph 2.2), the experimental results of a MPhC 3D strip cavity (Paragraph 2.3), the MPhC 3D wide cavity devoted to optical trapping in air (Paragraph 2.4) and the MPhC 3D wide cavity devoted to optical trapping in water (Paragraph 2.5).

Finally, Chapter 3 (“Mesoscopic Photonic Crystal waveguides”) is devoted to the analysis of the MPhC 3D strip and 3D wide waveguides. The evaluation of the influence of the gaussian source waist on the collimation phenomenon (Paragraph 3.2) and the analysis of the MPhC 3D wide waveguide with tilted source (Paragraph 3.3) are also illustrated.

These last results opens the way for developing a full class of routing elements that can be combined together taking advantage of the spatial and spectral reconfigurability that MSC offers.

# 1. MESOSCOPIC PHOTONIC CRYSTALS

## 1.1 *Mesoscopic Photonic Crystals State of Art*

The optical beam propagation without distortion and lateral spreading inside a structure is called Self-Collimation (SC) [1]. This phenomenon has been proved in Photonic Crystals (PhCs) and metamaterials for Bessel-like beams and for arbitrary beams [2], and it has become a powerful tool for different fields that include light guiding and routing thanks to the anisotropic dispersion of periodic structures [3].

This phenomenon is an alternative of the typical confining mechanisms, for example bandgaps or index guiding, since it happens in flat regions of Photonic Crystal (PhC) band structures: the energy flows in a fixed direction without lateral dispersion thanks to the group velocity vector that, for topological reasons, remains constant for a wide range of wavevectors. The traditional Photonic Crystals allow obtaining efficient SC only in highly symmetric direction for the lattice and not in arbitrary directions. For this reason, fixed key design parameters are required, allowing for only few degrees of freedom and extreme difficulty to combine in the same structure SC with other optical effects.

SC phenomenon in two-dimensional (2D) PhCs has been demonstrated both theoretically and experimentally, firstly, in 1999 by Kosaka [3] and, after this work, there were many studies both theoretical [4-11] and experimental [12]. Several 2D PhC devices based on SC have been demonstrated both theoretically, such as waveguide [13, 14], invisibility cloak medium [15], Mach-Zehnder interferometer [16-18], optical junction [19], bend [20, 21], splitter [22, 23], optical switch [24], cavity [25, 26], filter [27] and experimentally, such as in-plane splitting coupler [28], reconfigurable optical switch [29], splitter[30, 31], quantum walks [32], Mach-Zehnder interferometer [33, 34], cavity [35]. Furthermore, SC has been at the heart of a 3D PhC bend experimentally demonstrated [36].

Recently, SC phenomenon has been proved also in metamaterials both theoretically [37], in one dimensional (1D) PhCs combining positive and negative index layers and

experimentally [38], by alternating stripe layers of negatively refracting (PhCs) and positively refracting (air) materials.

Also other periodic structures different from PhCs allow SC, such as sonic crystals [39-41], plasmonic crystals [42-44] and array of the periodically drilled holes interacting with liquids [45].

In this scenario, Mesoscopic PhCs (MPhCs) have attracted the interest of research as possible alternative of the traditional PhCs since they avoid SC limitations [46-49]. The MPhCs support the Mesoscopic SC (MSC) phenomenon to achieve 'guideless' waveguiding in linear media and that can be reached by engineering their angular anisotropy [50]. A MPhC is a 1D periodic superstructure that can be realized by cascading slabs of different materials (or metamaterials) showing opposite spatial dispersion, such as traditional PhCs and slabs of bulk materials [46, 47, 51]. On the base of the spatial dispersion engineering, for a given direction, MSC is obtained when the focusing properties of the PhC slabs compensate the natural defocusing of the bulk material slabs. The 'guideless' waveguiding paves the way for the conception of structures showing discrete (vertical) translational invariance. In these MPhC 2D structures a coexistence of several physical effects can occur, thanks to the many degrees of freedom [1]: input facet impedance perfect matching [46], stable Fabry-Pérot-like microcavities having flat parallel mirrors with an improved reflectivity able to reflect even non-paraxial beams, as curved mirrors do [47, 52-54], slow light waveguides [50], compensation of time and space dispersion to achieve linear solitons [55].

At the same time, MPhCs can be exploited to design a full novel class of MSC based devices, such as high sensitivity and Q-factor 2D microcavities [47, 56].

Recently, different approaches have been proposed to suppress optical diffraction. For example, this goal was achieved experimentally, enhanced by transverse Anderson localization, in chip-scale dispersion-engineered anisotropic media [57]. However, this approach requires complex photonic crystal superlattice structure by modifying the geometry of more than 4,000 scatterers in the superlattice.

In order to verify the performance variations of the MPhC 2D and 3D structures, I have

designed and analysed MPhC 3D waveguides and cavities. The analysis of 3D structures is very complex and onerous from the point of view of required memory and calculation time, but it is necessary when we want to carry out a realistic design of structures for sensoring, optical trapping in air or in water especially of nanometric particles, and routing and to obtain MSC along tilted direction.

## 1.2 *Mesoscopic Photonic Crystals Applications*

### 1.2.1 *Refractive index sensor*

Refractive index sensing has become a powerful tool for different fields that include physical, chemical and biological parameter detection. The nanotechnology progress allows the fabrication of high performance resonant sensors based on different geometrical configurations such as ring resonators, microstructured optical fibers and plasmonic sensors [58-60] to mention a few.

In the last years, Photonic Crystals (PhCs) have been largely exploited to realize high performance refractive index sensors in different configurations such as line defect, point cavity and Mach-Zehnder interferometer [61-64].

In this scenario the MPhCs pave the way for the conception of structures showing discrete (vertical) translational invariance. Hence, MPhCs can be exploited to design a full novel class of MSC based devices, such as high sensitivity and Q-factor microcavities inheriting the translational invariance property. The strong near field localized within the 2D cavity and the translational invariance, demonstrated in [47, 56], make this structure be fitting for devices able to tweeze-and-sense micro- and nano-object systems. Furthermore, being its properties mainly topological (and less related to material properties), it can be easily adapted to be fabricated by means of well-established technological solutions (GaAs membranes, SOI, etc.) that can be integrated in microfluidic systems and labs-on-chip.

I have designed and analysed refractive index sensors based on MPhC 2D and 3D strip microcavities, that exhibit high quality-factor and good sensitivity. Moreover, these results pave the way for a new class of highly compact refractive index sensors, where the translation invariance property may be used for addressing different analytes on the same sample. The high near-field localised within the cavity is suitable for optical tweezing applications, where the translational invariance may allow for linear repositioning of the trapped objects.

### 1.2.2 *Optical trapping in air and in water*

Optical trapping and manipulation (OTM) has become a widely utilized, non-invasive tool for the optical control of nano-objects. Usually the OTM refers to biological applications where living cells, nano-particles and DNA strands are placed, identified and modified [65-67]. To this end, different technologies have been developed to increase trapping efficiency as optoelectronic- [68], plasmonic- [69-72] and solid core waveguide-based tweezers [73].

In this scenario, photonic crystals have become a key technology for light trapping and photon manipulation [74] and efficient and enhanced optical trapping for small particles has been demonstrated in both the near field [75] and far field [76].

Till now, efforts in OTM mostly concerned particles dispersed in liquid environments. OTM of air particulate is more challenging mainly because of their faster Brownian dynamics and reduced heat dissipation. Air (and water) pollutants can be in the form of harmful particulate matter (PM) which may have devastating impact on health and on the ecosystem. PM are directly emitted to the atmosphere or can be formed as the outcome of complex reaction of precursor chemicals. Source of direct PM and PM precursors are households, industries, vehicles, agriculture, waste management, and power plants. Achieving a platform allowing the tweezing of fine particulate in air is therefore mandatory for the analysis of indoor and outdoor air quality, in order to increase the knowledge of PM origin, vehiculation and distribution.

Since the early pioneering work of Ashkin and associates [77-79], two main approaches for OTM of micron- or nano-sized aerosol particles have been exploited: the former based on the radiation pressure and gradient force for trapping transparent or low-absorbing particles, and the latter based on the so-called “photophoretic force” for trapping high absorbing particles [80-83].

I have designed and analysed high performance MPhC 3D wide microcavities for optical trapping of fine particulate matter in air and in water, exhibiting high-Q and 3D-light confinement. Moreover, it has been numerically demonstrated the efficiency of the MPhC 3D wide microcavities for optical trapping in air and in water, exploiting the

aforementioned approach based on the radiation pressure and gradient force: it is possible to obtain very high trapping potential for polystyrene particles having radii as small as 245 nm in air and 200 nm in water. The obtained results are extremely encouraging since it is possible to obtain extremely deep optomechanical potential well (about 4 times in air and 5 times in water, bigger than the minimum requirement for trapping) allowing for stable trapping, and opening the way for novel configurations for optical trapping of nano- and micro-particles, over areas of ~10×10 $\mu m^2$ in air and in water, that could be linearly repositioned exploiting the translational invariance of the MPhC microcavity along the transverse direction.

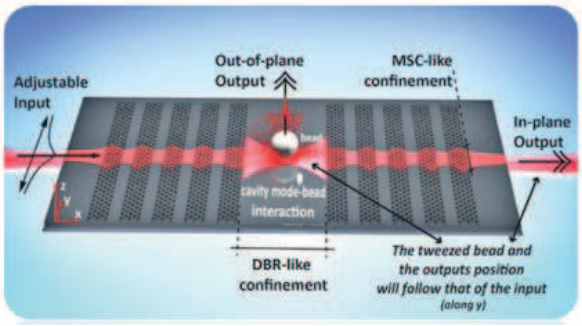


Fig. 1.1: Operation of the mesoscopic optical trapping: light source (red arrow), vertical shift of the light source (black arrows), object able to interact with the localised mode in the microcavity (white sphere).

## 1.3 *Mesoscopic self-collimation principle*

### 1.3.1 *Propagation inside an isotropic or anisotropic medium*

A plane wave propagating within an isotropic medium (like as the slab of bulk material) has the wavevector **k** parallel to the Poynting vector **S** = 1/2 **E** $\times$ **H**$^*$, the equiphase wavefronts always perperdicular to wavevector **k**, the propagation direction always parallel to **S**, **S** always parallel to the group velocity vector $\mathbf{v_g}$, the phase velocity vector $\mathbf{v_f}$ parallel to **k**, and the isofrequency curves (IFCs) in the *k*-space circular (Fig. 1.2a) [54] [84]. Then, **S**, $\mathbf{v_g}$ and **k** are parallel.

A plane wave propagating within an anisotropic medium (like as the slab of hole-type square lattice PhC), at a given angular frequency $\omega$, has the wavevector **k** not parallel to the Poynting vector **S**, the equiphase wavefronts always perperdicular to wavevector **k**, the propagation direction always parallel to **S**, **S** always parallel to the group velocity vector $\mathbf{v_g}$, the phase velocity vector $\mathbf{v_f}$ parallel to **k**, and the isofrequency curves (IFCs) in the *k*-space not circular but with a generic shape (Fig. 1.2b). Then, **S** and $\mathbf{v_g}$ are parallel, instead **k** is, in general, not parallel to **S** and $\mathbf{v_g}$.

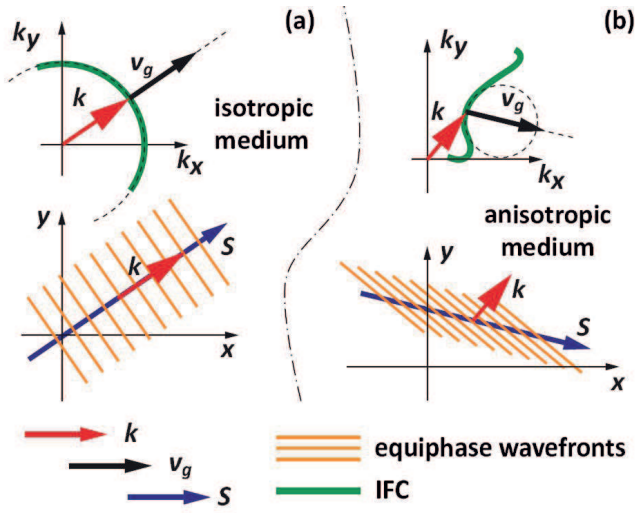


Fig. 1.2: A plane wave propagating within an (a) isotropic and (b) an anisotropic media. The wavevector (red arrow), the Poynting vector (blue arrow), the equiphase wavefronts (orange parallel lines), the group velocity vector (black arrow), the IFC in the *k*-space (thick green curve) and the osculator circle of the corresponding IFC for a particular *k*-point (dashed circumference) are represented [54].

An IFC in the *k*-space is the locus defined by the head of the wavevector as a function of the direction. The propagation of infinite plane waves in all directions and their corresponding phase velocities $\mathbf{v_f}$ allow to retrieve the IFC. In fact, the wavevector **k** is equal to:

$$\mathbf{k}(\omega) = k_0 n_{eff}(\omega, \theta)\mathbf{a_k} = \omega / \mathbf{v_f}(\omega) \quad (1.1)$$

where $k_0 = \omega/c$ is the wavenumber in vacuum, $c$ is the phase velocity of light in vacuum, $n_{eff}$ is the effective refractive index, $\theta$ is the angle of **k**, $\mathbf{a_k}$ is the unit vector parallel to **k**.

Within an isotropic medium, the $n_{eff}$ is constant and equal to its refractive index.

The group velocity is the gradient of the bandstructure with respect to the wavevector ($\mathbf{v_g} = \nabla_{\mathbf{k}} \omega(\mathbf{k})$) and, then, it is normal to the IFC.

### 1.3.2 *The index of curvature*

The IFC in the *k*-space of an isotropic medium is a $\Gamma$-point centred circumference with circle radius $\rho$ equal to the wavevector **k** (Fig. 1.2a). The *curvature* $G$ of the IFC is $1/\rho$. Then, the effective refractive index $n_{eff}$ of the isotropic medium is $n_{eff} = |\mathbf{k}|/k_0 = \rho/k_0 = 1/(Gk_0)$, and it describes the behaviour of light in all the directions.

The IFC in the *k*-space of an anisotropic medium has a generic shape defined by the variation of the wavevector **k** (Fig. 1.2b). For a given point of the IFC it can be defined an osculating circle (Fig. 1.2b), an osculating circle radius $\rho$, and a local index, called curvature index $n_c$, equal to $n_c = \rho/k_0 = 1/(Gk_0)$ which describes the behaviour of light in a given direction [50, 54, 55]. In particular, the curvature index $n_c$ is [54, 85]:

$$n_c = \rho / k_0 = 1 / \{k_0[\nabla(\nabla\omega / |\nabla\omega|)]\} \quad (2.1)$$

### 1.3.3 *Propagation through a bulk medium/PhC interface*

Considering a plane wave impinging a system with a *discrete translational*

*invariance* (that is a bulk medium/PhC interface) from the bulk medium side at a given frequency, the Bloch theorem involves that any transmitted or reflected wave must conserve the component $\mathbf{k}_{//}$ of the impinging wavevector $\mathbf{k}$ parallel to the interface, except for integer multiples of the reciprocal lattice vectors [54, 86].

Let us consider two IFCs with *curvatures*, that have opposite sign, of an isotropic bulk medium and of a birefringent PhC, respectively, obtained by projecting the respective band diagrams on the k-plane and considering the same frequency (Fig. 1.3a).

The impinging angle $\theta_{kb}$ of the plane wave from the bulk medium side is given by its wavevector $\mathbf{k_b}$ (Fig. 1.3(a) and (b)). $\theta_{kb}$ is equal to $\theta_{vb}$ because $\mathbf{k_b}$ is parallel to the group velocity $\mathbf{v_{g,b}}$.

Only considering the transmitted wave through the system with a *discrete translational invariance*, the wavevector $\mathbf{k_c}$ inside the PhC is obtained by projecting $\mathbf{k_b}$ on the PhC IFC along the direction normal to the interface (Fig. 1.3(a) and (b)). $\mathbf{k_c}$ forms an angle $\theta_{kc}$ with respect to the *x*-axis. The propagation direction inside the PhC is the direction of the PhC group velocity vector $\mathbf{v_{g,c}}$ that forms an angle $\theta_{vc}$ with respect to the *x*-axis.

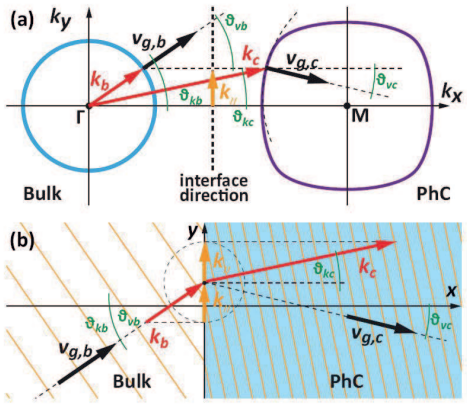


Fig. 1.3: (a) IFCs of an isotropic bulk medium (blue thick circle) and of a birefringent PhC (violet thick curve) on the same k-space. The interface direction (dashed line) is parallel to $k_y$. The group velocity vector (black arrow), the wavevector (red arrow), the wavevector component parallel to the interface (orange arrow), the angle formed by each vector with respect to the *x*-axis (green arc), and the equiphase wavefronts (orange lines) are represented. (b) A plane wave impinging on a bulk medium/PhC interface from the side of the bulk medium [54].

The IFC *curvature* can be *positive* or *negative* depending on the position of the wavevector **k** with respect to the osculator circle. In particular for a given point of the IFC in the *k*-space and the corresponding osculator circle in the given point, the IFC *curvature* is *positive* if **k** is inside the osculator circle or intersects it in two points (as for example in bulk medium of Fig. 1.3a); *negative* if **k** is completely outside the osculator circle (as for example in PhC medium of Fig. 1.3a).

The Mesoscopic Self-Collimation can be obtained by cascading two slabs of different materials, showing *opposite curvature*, that compensate their opposite lateral dispersion.

An isotropic medium (like as the slab of bulk material) has always *positive curvature* (positive lateral dispersion), because **k** is always inside the osculator circle.

An anisotropic medium (like as the slab of hole-type square lattice PhC) can have *positive* or *negative curvature* (positive or negative lateral dispersion). Increasing the PhC refractive index contrast, the PhC anisotropic band diagram undergoes a deformation moving away from the isotropic case (Fig. 1.4).

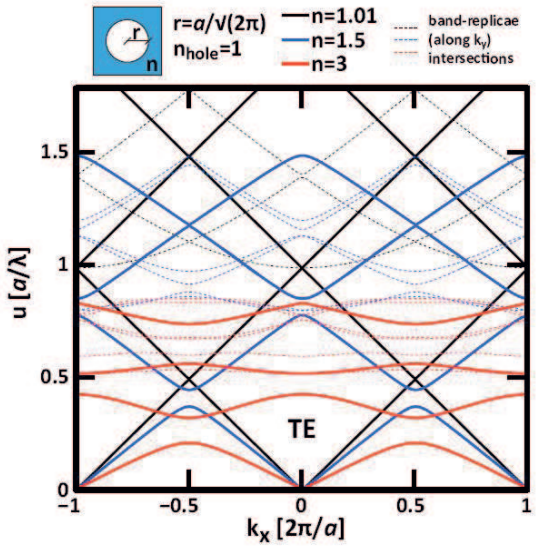


Fig. 1.4: The intersections between the ($k_y$ = 0)-plane with the first four bands of the TE band diagram of a 2D unitary cell of a hole-type square lattice PhC, for $n_{hole}$ = 1 and $n_{eff\_bulk}$ = 1.01, 1.5, 3. The first four bands belonging to the FBZ (solid thick lines) and the intersections of the same bands belonging to the adjacent Brillouin zones along the $k_y$-direction (the dashed thin lines) are represented. The hole has the same area of the bulk within the PhC unitary cell (hole radius $r = a/\sqrt{(2\pi)}$ and lattice constant $a$) [54].

### 1.3.4 *Mesoscopic Self-Collimation condition*

To obtain the Mesoscopic Self-Collimation the accumulated *mean curvature* over one mesoscopic period D should be zero, considering the propagation along the high symmetry *x*-direction of a gaussian source with waist $w_0$ [50, 54, 55]:

$$\langle \frac{1}{n_c} \rangle = \frac{1}{D} \int_0^D \frac{dl}{n_c(l)} = 0 \tag{3.1}$$

We consider a MPhC in which each mesoperiod is obtained by interleaving focusing slab constituted by hole rows of a 45°-tilted hole-type square-lattice PhC (having hole radius *r*, overall width $d_c$ and lattice constant *a*), and defocusing slab constituted by bulk material having a effective refractive index $n_b$ and a width $d_b$ (Fig. 1.5). The whole mesoperiod is etched on a membrane. Along the *x*-direction and the *y*-direction of the PhC slab the centers of holes are distant $\sqrt{2}\times a$ from each other. Along the *x*-direction the PhC slab has a length $a/(2\sqrt{2})$ before the center of the first hole and after the center of the last hole.

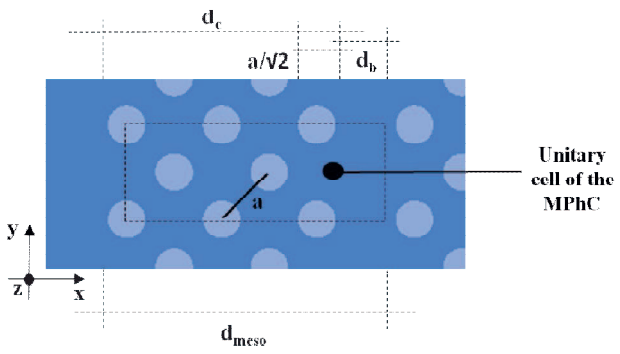


Fig. 1.5: Sketch of an example of MPhC mesoperiod: focusing slab constituted by hole rows of a 45°-tilted hole-type square-lattice PhC and defocusing slab constituted by bulk material.

To obtain the Mesoscopic Self-Collimation in the considered MPhC, the Eq. 3.1 becomes:

$$\frac{1}{D}\left(\frac{d_c}{n_c(u)} + \frac{d_b}{n_b}\right) = 0 \tag{4.1}$$

where $n_c(u)$ is the curvature index of the PhC unitary cell along the ΓM-direction and $u = a/\lambda$ is the central normalized frequency of the gaussian source.

In MPhCs it is possible to combine MSC with other properties, because the MSC condition is independent of the mesoperiod $D = d_c + d_b$ and of the effective refractive index $n_{eff}(u)$ of the PhC.

For example, considering $n_b = 2.90$, air holes and $r$ = 0.28×a, and evaluating $n_c(u)$, several solutions ($d_b$, $d_c$, u) of the Eq. 4.1 have been obtained (Fig. 1.6).

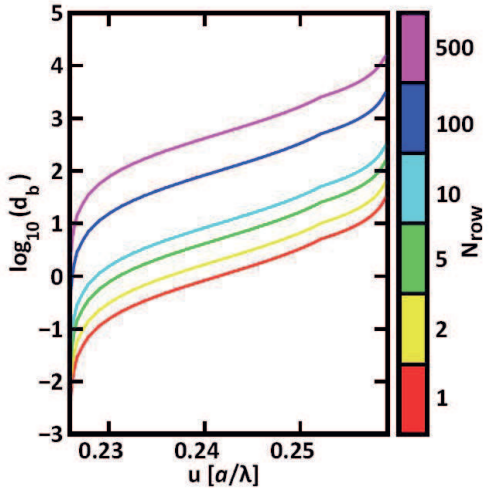


Fig. 1.6: The bulk width $d_b$ (in logarithmic scale) that ensures MSC as a function of the normalized frequency $u$, for several values of the number of PhC hole rows $N_{row}$ (that is the PhC width $d_c$), considering, for example, $n_b = 2.90$, air holes and $r$ = 0.28×a [54].

## 1.4 *The 2D and 3D designs of the geometries of the single MPhC multilayers*

The design of 2D and 3D geometries of the single MPhC multilayers were performed by means of the 2D Plane Wave Expansion Method (2D-Mit Photonic-Bands software [87]) and 3D Plane Wave Expansion Method (3D-MPB software), respectively.

### 1.4.1 *Properties of the 2D and 3D unitary cells of PhCs*

The 3D design of the geometry of the single MPhC multilayer starts from the calculation of the map of the isofrequential curves (IFCs) of a 3D unitary cell of PhC for the first TE band, that is the band diagram projected in the $k_x$-$k_y$ plane.

The 3D-FDTD LUMERICAL software allows to calculate (in the kf plane) the graphs of the band diagrams obtained at the values that k assumes along Γ-X, X-M, M-Γ. Moreover, the 3D-FDTD LUMERICAL software allows to obtain, in linear scale and in logarithmic scale, for the TE modes of a 3D unitary cell of PhC, the frequency spectra as a function of k, that is in the kf plane the values of the ordinates of the points of the frequency spectra.

The 3D Mit Photonic-Bands (MPB) software allows to calculate the isofrequential curves (IFCs), that is the band diagram in the $k_x$-$k_y$ plane.

In first approximation a 2D unitary cell of PhC has been designed and analysed [46, 54] to define the geometries of the single MPhC multilayers of the 3D cavities and waveguide.

The design and the analysis of the 2D unitary cell of PhC is reported in [46, 54].

Fig. 1.7 shows the map of the isofrequential curves (IFCs) of the 2D-unitary cell of an infinite square-lattice PhC characterized by a air hole radius r = 0.28×a, a lattice constant *a* and a GaAs bulk membrane effective refractive index $n_b$=2.90, for the first TE band, obtained by means of 2D-MPB. The black line shows a single zero-curvature point at its centre that corresponds to the PhC self-collimation frequency $u_{sc}$. Due to the symmetry, only a quarter of the FBZ has been considered to describe the 2D-unitary cell properties of PhC. The figure shows that along the Γ-M-direction, as the frequency increases, the radius of the osculating circle becomes bigger and the curvature is

positive. At the critical IFC, the radius becomes infinite and the curvature is zero. Exceed this critical IFC, the curvature becomes negative and its modulus becomes lower.

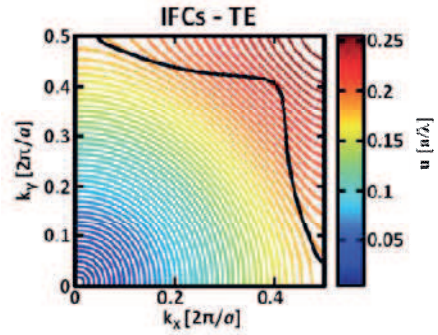


Fig. 1.7: IFCs-diagram of the 2D PhC unitary cell: the band diagram projected on the k-plane. The thick black curve represents the zero-curvature locus, that corresponds to the PhC self-collimation frequency [54].

Fig.1.8 shows (a) the effective refractive index $n_{eff}$ and (b) curvature index $n_c$, evaluated by the map of isofrequential curves of the 2D unitary cell of the square-lattice PhC along the ΓM-direction, as a function of the normalized frequency u, calculated for the first TE band. The Γ-X-direction of the MPhC corresponds to the Γ-M-direction of the unitary cell of PhC, since the MPhC consists of a 45°-tilted PhC. The curvature index $n_c$ is positive and small for lower frequencies and diverges to an infinite value at the normalized frequency $u_{sc}$=0.2272×a/λ. Exceed this frequency, the curvature index $n_c$ becomes negative and its absolute value decreases.

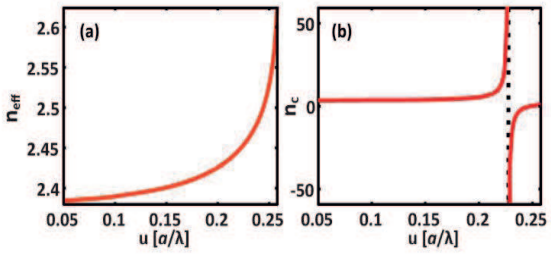


Fig. 1.8: (a) Effective refractive index $n_{eff}$ and (b) curvature index $n_c$, as a function of the normalized frequency u, calculated for the first TE band of the 2D unitary cell of a square-lattice PhC [46] [54].

Then, to define the geometries of the single MPhC multilayers of 3D cavities for optical bio-trapping in water, I have designed and analysed different 3D unitary cells of

PhCs in water: GaAs, Si and Si on $SiO_2$ 3D unitary cells of PhCs, with holes filled by air or water, having hole radius r = 0.25×a and lattice constant $a$ = 350nm. The membrane thicknesses are 250nm, 240nm, 260nm, respectively.

Fig. 1.9 shows the map of the isofrequential curves (IFCs) of the aforementioned GaAs 3D-unitary cell of an infinite square-lattice PhC in water, for the first TE band, obtained by means of 3D-MPB. The water refractive index is n=1.33, the bulk refractive index is equal to $n_{GaAs}$ = 3.355 and the hole is filled by water. The black line corresponds to the IFC showing a null curvature. The black line, showing a flat region, corresponds to the PhC self-collimation frequency. Due to the symmetry, only one quarter of the FBZ has been considered to describe the 3D-unitary cell properties of PhC. The figure shows that along the Γ-M-direction, as the frequency increases, the radius of the osculating circle becomes bigger and the curvature is positive. At the critical IFC, the radius becomes infinite and the curvature is zero. Exceed this critical IFC, the curvature becomes negative and its modulus becomes lower.

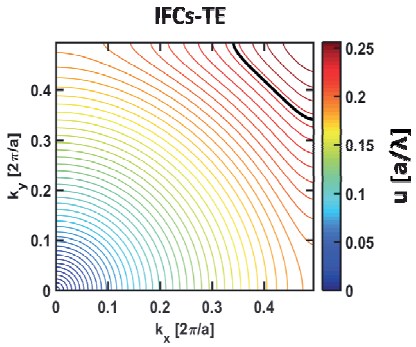


Fig. 1.9: IFCs-diagram of the GaAs 3D PhC unitary cell in water: the band diagram projected on the k-plane. The thick black curve represents the zero-curvature locus, that corresponds to the PhC self-collimation frequency.

Fig.1.10 shows (a) the effective refractive index $n_{eff}$ and (b) curvature index $n_c$, evaluated by the map of isofrequential curves of the aforementioned GaAs 3D unitary cell of the square-lattice PhC in water along the ΓM-direction, as a function of the normalized frequency u, calculated for the first TE band. The Γ-X-direction of the MPhC corresponds to the Γ-M-direction of the unitary cell of PhC, since the MPhC

consist of a 45°-tilted PhC. The curvature index $n_c$ is positive and small for lower frequencies and diverges to an infinite value at the normalized frequency $u_{sc}$=0.2339×a/λ. Exceed this frequency, the curvature index $n_c$ becomes negative and its absolute value decreases.

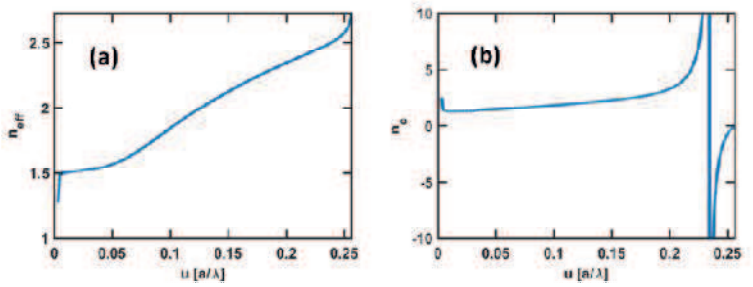


Fig. 1.10: (a) Effective refractive index $n_{eff}$ and (b) curvature index $n_c$, as a function of the normalized frequency u, calculated for the first TE band of the GaAs 3D unitary cell of a square-lattice PhC in water.

Then, to define the geometries of the single MPhC multilayers of 3D cavities and waveguide in air, I have designed and analysed different 3D unitary cells of PhCs in air.

Fig. 1.11 shows the map of the isofrequential curves (IFCs) of the aforementioned GaAs 3D-unitary cell of an infinite square-lattice PhC in air, for the first TE band, obtained by means of 3D-MPB. The bulk refractive index is equal to $n_{GaAs}$ = 3.4, the hole radius is r = 0.28×a, the lattice constant is $a$ = 360nm and the membrane thickness is 270nm. The black line corresponds to the IFC showing a null curvature. The black line, showing a flat region, corresponds to the PhC self-collimation frequency. Due to the symmetry, only one quarter of the FBZ has been considered to describe the 3D-unitary cell properties of PhC. The figure shows that along the Γ-M-direction, as the frequency increases, the radius of the osculating circle becomes bigger and the curvature is positive. At the critical IFC, the radius becomes infinite and the curvature is zero. Exceed this critical IFC, the curvature becomes negative and its modulus decreases.

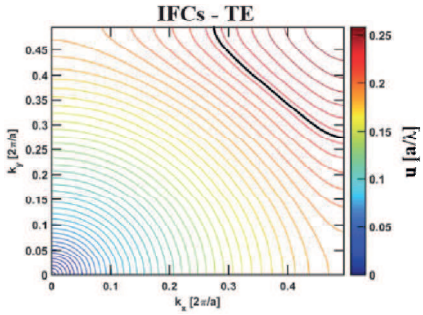


Fig. 1.11: IFCs-diagram of the GaAs 3D PhC unitary cell in air: the band diagram projected on the k-plane. The thick black curve represents the zero-curvature locus, that corresponds to the PhC self-collimation frequency.

Fig.1.12 shows (a) the effective refractive index $n_{eff}$ and (b) curvature index $n_c$, evaluated by the map of isofrequential curves of the aforementioned GaAs 3D unitary cell of a square-lattice PhC in air along the ΓM-direction, as a function of the normalized frequency u, calculated for the first TE band. The Γ-X-direction of the MPhC corresponds to the Γ-M-direction of the unitary cell of PhC, since the MPhC consist of a 45°-tilted PhC. The curvature index $n_c$ is positive and small for lower frequencies and diverges to an infinite value at the normalized frequency $u_{sc}=0.2254\times a/\lambda$. Exceed this frequency, the curvature index $n_c$ becomes negative and its absolute value decreases.

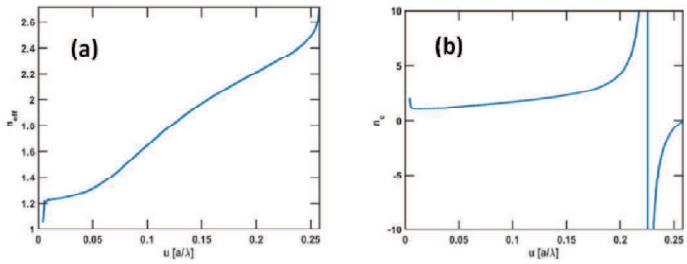


Fig. 1.12: (a) Effective refractive index $n_{eff}$ and (b) curvature index $n_c$, as a function of the normalized frequency u, calculated for the first TE band of the GaAs 3D unitary cell of a square-lattice PhC in air.

### 1.4.2 *Tailored overall reflectivity*

The Mesoscopic Photonic Crystals allow to obtain Mesoscopic Self-Collimation and tailored Reflectivity at the same time. In fact, the Mesoscopic Self-Collimation

condition (Eq. 4.1) permits an infinite number of solutions and, moreover, the Mesoscopic Photonic Crystal can be designed as a 1D anti-reflection or high-reflection multilayer. In particular, the MSC condition is independent on the mesoperiod $D = d_c + d_b$ and on the effective refractive index $n_{eff}(u)$ of the PhC. Moreover, as in the Distributed Bragg Reflectors (DBRs), in the MPhCs it is possible to determine $d_c$ and $d_b$ that allow to obtain anti-reflection or high-reflection multilayer.

A MPhC waveguide has to satisfy, at the same time, the MSC condition and the Anti-Reflection (AR) multilayer design rule (both PhC and bulk slices equal to a quarter-wave film), and shows minimal unwanted reflections at PhC input interfaces without either affecting the feasibility or the complexity of the structure.

A MPhC mirror has to satisfy, at the same time, the MSC condition and the High-Reflection (HR) multilayer design rule.

Then the single AR or HR MPhC multilayer has to satisfy the system of algebraic equations (Eq. 5.1), where the first one represents the MSC condition while the second and the third equations represent the single AR multilayer condition, if (m,p) are even integers, and the single HR multilayer condition, if (m,p) are odd integers:

$$\begin{cases} d_c/n_c(u) + d_b/n_b = 0 \\ d_b n_b = m\lambda/4 = ma/(4u) \\ d_c n_{eff}(u) = p\lambda/4 = pa/(4u) \end{cases} \tag{5.1}$$

In these equations $n_{eff}(u)$ is the PhC phase index, $n_c(u)$ is the PhC curvature index, u is the central source normalized frequency ($u = a/\lambda$), $a$ is the lattice constant of the PhC, $d_c$ is the length of the PhC slab, $d_b$ is the length of the bulk material slab, $n_b$ is the bulk membrane effective refractive index.

#### 1.4.2.1 *Single AR and HR MPhC multilayers searching algorithm*

The single AR or HR MPhC multilayer has to satisfy the system of algebraic equations (Eq. 5.1). The evaluation of the effective refractive index $n_{eff}(u)$ and curvature index $n_c(u)$ of the PhC, described in previous paragraph 1.4.1, and the value of the bulk membrane effective refractive index $n_b$ allow to determine the triplets ($d_b$, $d_c$, u) that

satisfy the equation system (5.1).

The searching algorithm consists of three steps:

1) The length of the PhC slab $d_c$ is fixed. In particular, the number of rows of holes $N_{row}$ in the PhC is fixed ($d_c = aN_{row}\sqrt{2}/2$).
2) The pairs of values "length of the bulk material slab $d_b$" and the "normalized frequency *u*", that satisfy the MSC condition (the first equation of Eq. 5.1), are retrieved for each normalized frequency *u* above the PhC self-collimation frequency $u_{sc}$ obtained in previous paragraph 1.4.1.
3) From this set of solutions, the pairs of values "length of the bulk material slab $d_b$" and "normalized frequency *u*", that satisfy the single AR or HR multilayer condition (the second and the third equations of Eq. 5.1), are retrieved. Thus the triplets ($d_b$, $d_c$, u) that satisfy the equation system (5.1) are obtained.

Then the whole procedure is repeated for different values of $N_{row}$, that is for different values of $d_c$. For $N_{row} \leq 2$ there are no solutions ($d_b$, $d_c$, u), whereas for $N_{row} > 2$ there are several solutions increasing $N_{row}$.

In particular, the third step of the searching algorithm consists of four steps:

a) After the second step of the searching algorithm, two quantities $\tilde{m}$(u) and $\tilde{p}$(u) are calculated from the single AR or HR multilayer condition (the second and the third equations of Eq. 5.1).

$$\begin{cases} \tilde{m}(u) = \frac{4u}{a} d_b n_b \\ \tilde{p}(u) = 2\sqrt{2u} N_{row} n_{eff}(u) \end{cases} \tag{6.1}$$

b) The nearest integer approximation $m_{round}$(u) and $p_{round}$(u) for $\tilde{m}$(u) and $\tilde{p}$(u), respectively, are calculated.

Two errors $err_b$(u) and $err_c$(u) of the integer approximation $m_{round}$(u) and $p_{round}$(u), respectively, are defined as follows:

$$\begin{cases} err_b(u) = \tilde{m}(u) - m_{round}(u) \\ err_c(u) = \tilde{p}(u) - p_{round}(u) \end{cases} \tag{7.1}$$

c) The overall error err(u) of the two errors $err_b$(u) and $err_c$(u) is calculated:

$$err(u) = \sqrt{err_b(u)^2 + err_c(u)^2} \tag{8.1}$$

d) The pairs of values ($d_b$, u), that minimize the overall error err(u) of the integer approximation for m and p, are considered. Only if the integers m and p are both even or both odd, the triplets ($d_b$, $d_c$, u) are solutions of the equation system (5.1) i.e. represent the geometries of the single AR or HR MPhC multilayers, respectively.

To define the geometries of the single MPhC multilayers, in first approximation, of the 3D cavities and waveguide, the evaluation of the effective refractive index $n_{eff}(u)$ and curvature index $n_c(u)$ of the 2D unitary cell of PhC, described in Fig. 1.7 and in Fig. 1.8, and the value of the bulk membrane effective refractive index $n_b$ have been considered to determine the triplets ($d_b$, $d_c$, u) that satisfy the equation system (5.1) [46, 54].

Fig. 1.13 shows the set of retrieved solutions ($d_b$, $d_c$, u) of the equation system (5.1), considering the 2D PhC unitary cell, obtained by minimising the overall error of the integer approximation for m and p. The green and red triangles represent the AR (both m and p even) and HR solutions (both m and p odd), respectively. The thick green and red circles highlight the AR and HR MPhC multilayer geometries, respectively, fixed for the 3D cavities and waveguide. In particular, the green circle highlights the solution ($d_c$ = 3.536×a, $d_b$= 0.747×a, u = 0.2299 a/λ) and the red circle highlights the solution ($d_c$ = 9.192×a, $d_b$= 2.612×a, u = 0.2311 a/λ).

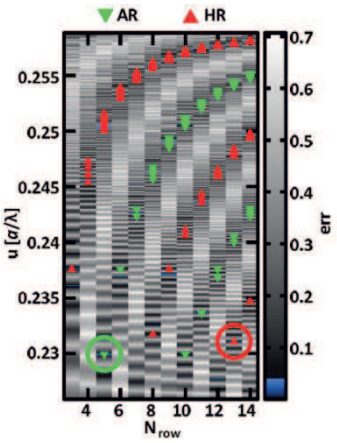


Fig. 1.13: Set of retrieved solutions of equation system (5.1), considering the 2D PhC unitary cell [54].

Then, to define the geometries of the single MPhC multilayers of 3D cavities for optical bio-trapping in water, the evaluation of the effective refractive index $n_{eff}(u)$ and curvature index $n_c(u)$ for each of the different 3D unitary cells of PhCs in water, described in Fig. 1.9 and in Fig. 1.10, and the value of the bulk membrane effective refractive index $n_b$ have been considered to determine the triplets ($d_b$, $d_c$, u) that satisfy the equation system (5.1).

Fig. 1.14 shows the set of retrieved solutions ($d_b$, $d_c$, u) of the equation system (5.1), considering the aforementioned GaAs 3D unitary cell of PhC in water, obtained by minimising the overall error of the integer approximation for m and p. The green and red triangles represent the AR (both m and p even) and HR solutions (both m and p odd), respectively. The thick red circle highlights the HR MPhC multilayer geometry that I have fixed for the 3D wide cavity in water. In particular, the red circle highlights the solution ($d_c$ = 9.192×a, $d_b$= 16.9992×a, u = 0.2463 a/λ).

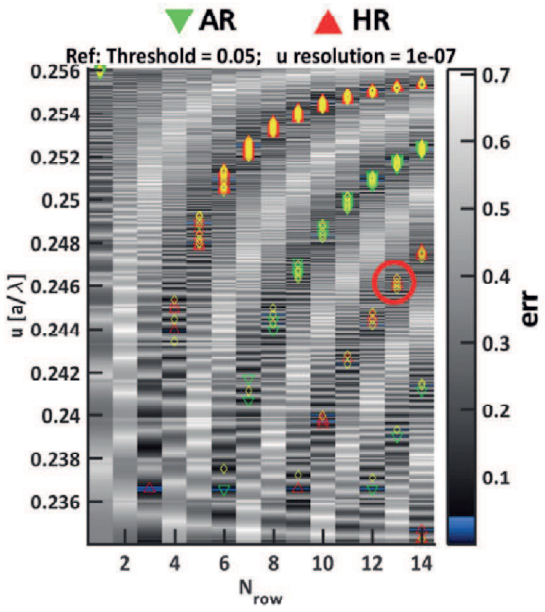


Fig. 1.14: Set of retrieved solutions of equation system (5.1), considering the GaAs 3D unitary cell of PhC in water.

Then, to define the geometries of the single MPhC multilayers of 3D cavities and waveguide in air, the evaluation of the effective refractive index $n_{eff}(u)$ and

curvature index $n_c(u)$ for each of the different 3D unitary cells of PhCs in air, described in Fig. 1.11 and in Fig. 1.12, and the value of the bulk membrane effective refractive index $n_b$ have been considered to determine the triplets ($d_b$, $d_c$, u) that satisfy the equation system (5.1).

Fig. 1.15 shows the set of retrieved solutions ($d_b$, $d_c$, u) of the equation system (5.1), considering the aforementioned GaAs 3D unitary cell of PhC in air, obtained by minimising the overall error of the integer approximation for m and p. The green and red triangles represent the AR (both m and p even) and HR solutions (both m and p odd), respectively. The thick green circle highlights the AR MPhC multilayer geometry that I have fixed for the 3D wide waveguide. In particular, the green circle highlights the solution ($d_c$ = 3.536×a, $d_b$= 3.1048×a, u = 0.2368 a/λ).

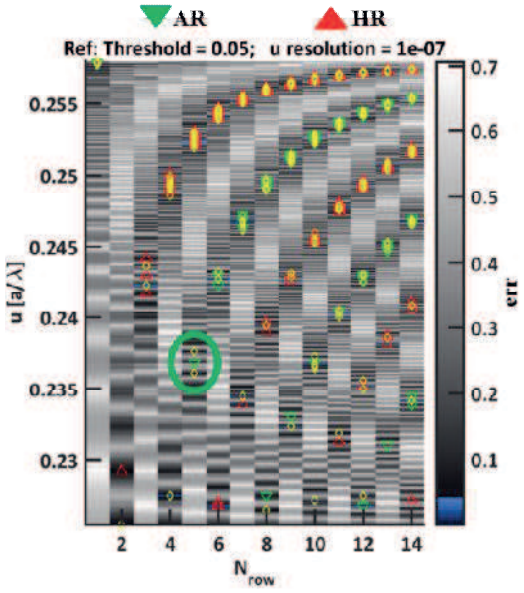


Fig. 1.15: Set of retrieved solutions of equation system (5.1), considering the GaAs 3D unitary cell of PhC in air.

# 2. MESOSCOPIC PHOTONIC CRYSTAL CAVITIES

## 2.1 *Mesoscopic Photonic Crystal 2D strip cavity devoted to refractive index sensor*

A refractive index sensor based on a mesoscopic photonic crystal 2D strip microcavity has been designed and analysed, that exhibits high quality-factor and good sensitivity [88, 89]. These results pave the way for a new class of highly compact index sensors, where the translation invariance property may be used for addressing different analytes on the same sample. Moreover, the high near-field localised within the cavity is suitable for optical tweezing applications, where the translational invariance may allow for linear repositioning of the trapped objects.

First, a mesoscopic photonic crystal 2D strip microcavity has been designed and analysed by means of 2D-FDTD calculation (MEEP). The design of the geometry of the single MPhC multilayer was performed by means of the 2D plane wave expansion method (2D-MPB), described in Fig. 1.13.

Fig. 2.1 shows the Fabry-Pérot cavity obtained by combining two 5-mesoperiod-long mesoscopic mirrors (MM). The whole device is etched on a 270 *nm*-thick membrane of GaAs ($n_{GaAs}$ = 3.4), fully surrounded by a dielectric analyte having refractive index *n* in the range 1.1-1.5. At telecom wavelength (1.55 $\mu m$), the effective refractive index $n_b$ of the fundamental mode supported by the membrane is equal to $n_b$ = 2.885, 2.890, 2.895, 2.900, 2.907 and 2.914, when *n* is 1, 1.1, 1.2, 1.3, 1.4 and 1.5, respectively. Each MM is obtained by interleaving focusing slabs constituted by 13 hole rows of a 45°-tilted hole-type square-lattice PhC (having hole radius $r = 0.28\times a$ and an overall width $d_c = 9.192\times a$, where *a* is the lattice constant), and defocusing slabs constituted by bulk material having a effective refractive index $n_b$ and a width $d_b = 2.612\times a$. The cavity defect has width $W=5.32\times a$.

Since the structure is periodic along the y-direction, showing a period $\sqrt{2}\times a$, periodic boundary conditions (PBCs) to the computational cell boundaries perpendicular to this direction have been imposed. PMLs are imposed at the boundaries perpendicular to the *x* direction. The structure is excited by injecting a broadband source ($1400nm < \lambda <$

1700*nm*) having a spatial distribution matching that of the fundamental TE mode (with the *x*-component of the electric field $E_x = 0$) of the membrane (at $\lambda = 1550nm$). The source is constant in the *y*-direction.

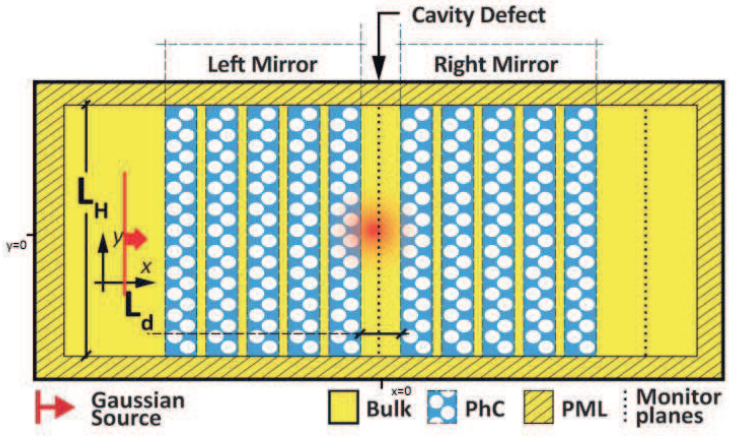


Fig. 2.1: Sketch of the mesoscopic photonic crystal 2D wide microcavity. In first approximation, the MPhC 2D strip microcavity has been designed and analysed.

For this structure, by means of 2D-FDTD calculation (MEEP), a numerical study on the influence of the analyte has been carried out, evaluating the transmission, reflection, "inside the cavity defect" and lateral losses spectra (normalized to the input power). An analyte having refractive index *n* equal to 1, 1.1, 1.2, 1.3, 1.4 and 1.5 has been considered, when the MPhC holes are filled by air or by the analyte.

Fig. 2.2 illustrates the normalized transmission spectra for *n* equal to 1, 1.3, 1.4 and 1.5, obtained for the structure having the MPhC holes fully filled by the analyte. When air (*n*=1) is considered as surrounding medium, the device exhibits a high Q-factor equal to 7888; equal to 4638 for *n*=1.3; equal to 3834 for *n*=1.4; equal to 2851 for *n*=1.5. The resonant peak within the bandgap, corresponding to the formation of a stable cavity mode, redshifts linearly as *n* increases. A lattice constant *a* equal to 360 nm is considered to locate the central wavelength of the gaussian source at about 1550 nm.

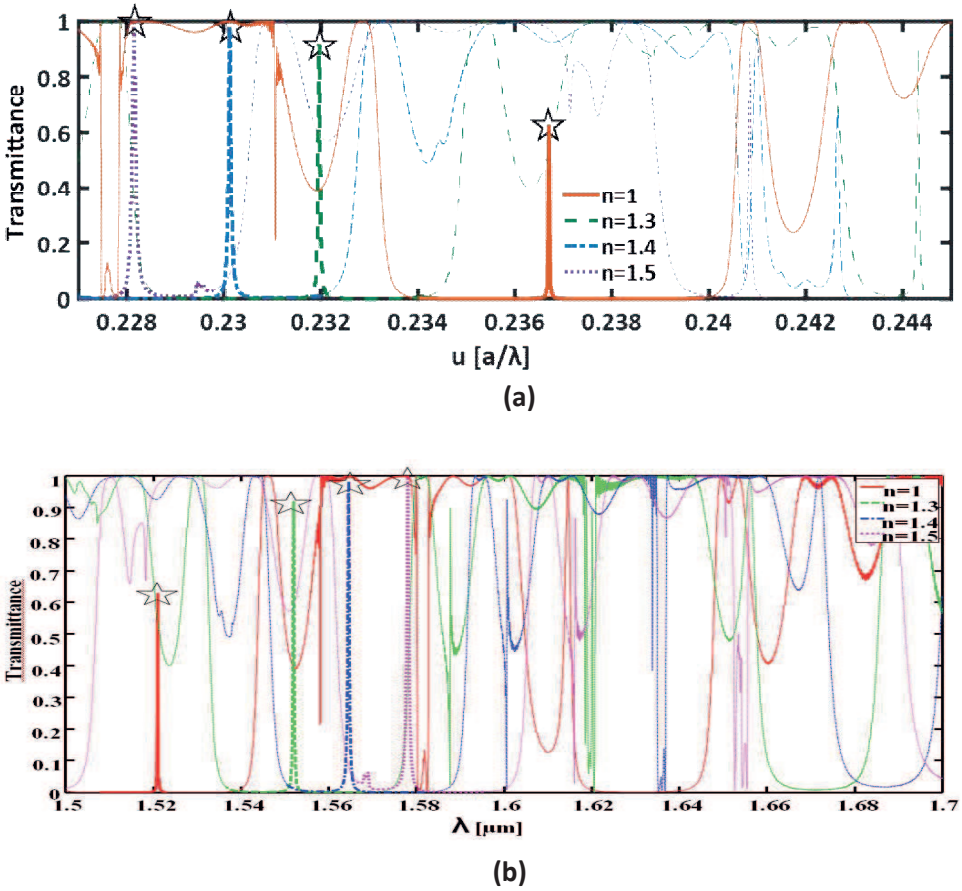


Fig. 2.2: Transmittance as a function of (a) the normalized frequency and (b) the wavelength, for $n_b$ = 2.8853 (solid red line), 2.9005 (dash green line), 2.9067 (dash dot blue line) and 2.9136 (dotted violet line), respectively, when the MPhC holes are filled by the analyte.

In order to investigate the nature of the modes, a second set of 2D-FDTD simulations (MEEP) were carried out where the total energy density was recorded in *xy*-plane at the resonant wavelength, considering *n* equal to 1, 1.1, 1.2, 1.3, 1.4 and 1.5 when the MPhC holes are filled by air or by the analyte.

Fig. 2.3 (a) and (b) depict, respectively, the profile of the total energy density as a function of the *x*-coordinate for $y = 0$ evaluated for the structure having $n = 1.3$ at the resonant wavelength (holes filled by the analyte), and the map of self-normalized total energy density (linear scale) in *xy*-plane evaluated for $n$=1.3 at the resonant wavelength (holes filled by the analyte). Fig. 2.3 (a) and (b) show the strong localization of energy in the cavity.

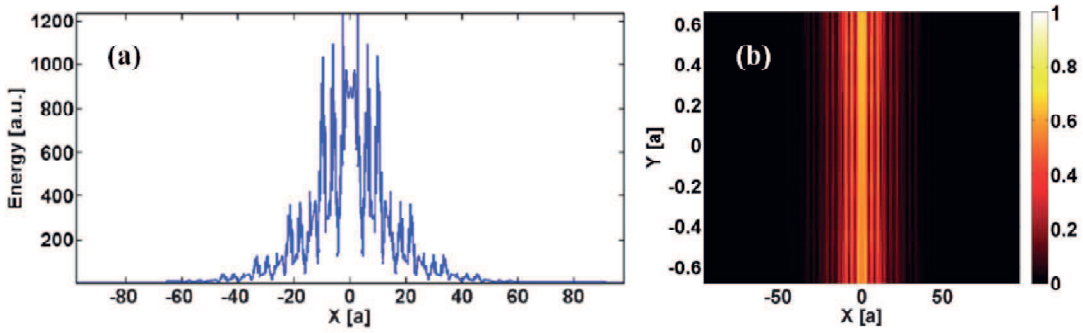


Fig. 2.3: (a) Profile of the total energy density as a function of the *x*-coordinate for $y = 0$, evaluated for the structure having $n = 1.3$ at the resonant wavelength (holes filled by the analyte); (b) Map of self-normalized total energy density (linear scale) in *xy*-plane, evaluated for n=1.3 at the resonant wavelength (holes filled by the analyte).

In order to evaluate the sensitivity, Fig. 2.4 shows the position of the resonant wavelength as a function of the analyte refractive index. The sensitivity of the sensor is $S=\Delta\lambda/\Delta n$ where $\Delta\lambda$ is the resonant wavelength shift and $\Delta n$ is the refractive index change of the analyte with respect to the air refractive index. The evaluated sensitivities are 28 and 112 nm/RIU (RIU: refractive index unit), respectively, when the MPhC holes are filled by air (blue line) or by the analyte itself (red line).

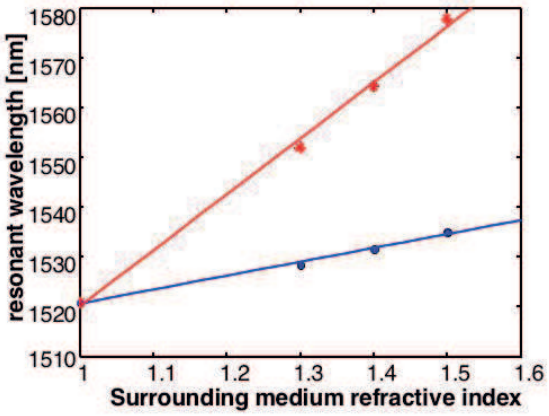


Fig. 2.4. Resonant wavelength as a function of the analyte refractive index: the blue and red lines correspond to a MPhC holes filled by air and by the analyte, respectively.

## 2.2 *Mesoscopic Photonic Crystal 3D strip cavity devoted to refractive index sensor*

A more realistic design considers a refractive index sensor based on a mesoscopic photonic crystal 3D strip microcavity.

The mesoscopic photonic crystal 3D strip microcavity has been designed and analysed by means of 3D-FDTD calculation (LUMERICAL). In first approximation, the geometry of the single MPhC multilayer of Fig. 1.13 has been considered.

The MPhC 3D strip microcavity has the same geometrical and physical parameters of the structure described in Fig. 2.1 and has a thickness (equal to 270 nm) and a bulk refractive index (equal to $n_{GaAs}$ = 3.4) and a superstrate and a substrate (that is a dielectric analyte having refractive index $n$ equal to 1, 1.3, 1.4 and 1.5). The PMLs are imposed at the boundaries perpendicular to the $z$ direction, a lattice constant $a$ is fixed (equal to 360 nm), the central wavelength of the gaussian source is fixed (equal to 1550 nm) and the source band is in the range $1400nm < \lambda < 1700nm$.

For this structure, a numerical study on the influence of the analyte has been carried out, evaluating the transmission, reflection, "inside the cavity defect" and out-of-plane loss spectra (normalized to the input power). An analyte having refractive index $n$ equal to 1, 1.3, 1.4 and 1.5 has been considered, when the MPhC holes are filled by the analyte.

Fig. 2.5 (a), (b) and (c) illustrate, respectively, the normalized transmission, reflection, and out-of-plane loss spectra for $n$ equal to 1, 1.3, 1.4 and 1.5, obtained for the structure having the MPhC holes fully filled by the analyte. When air ($n$=1) is considered as surrounding medium, the device exhibits a good Q-factor equal to 2631. As in the previous paragraph 2.1, the resonant peak within the bandgap, corresponding to the formation of a stable cavity mode, redshifts linearly as $n$ increases. Moreover, the resonant peaks are redshifted of about 60 nm compared to that of the 2D analysis (paragraph 2.1).

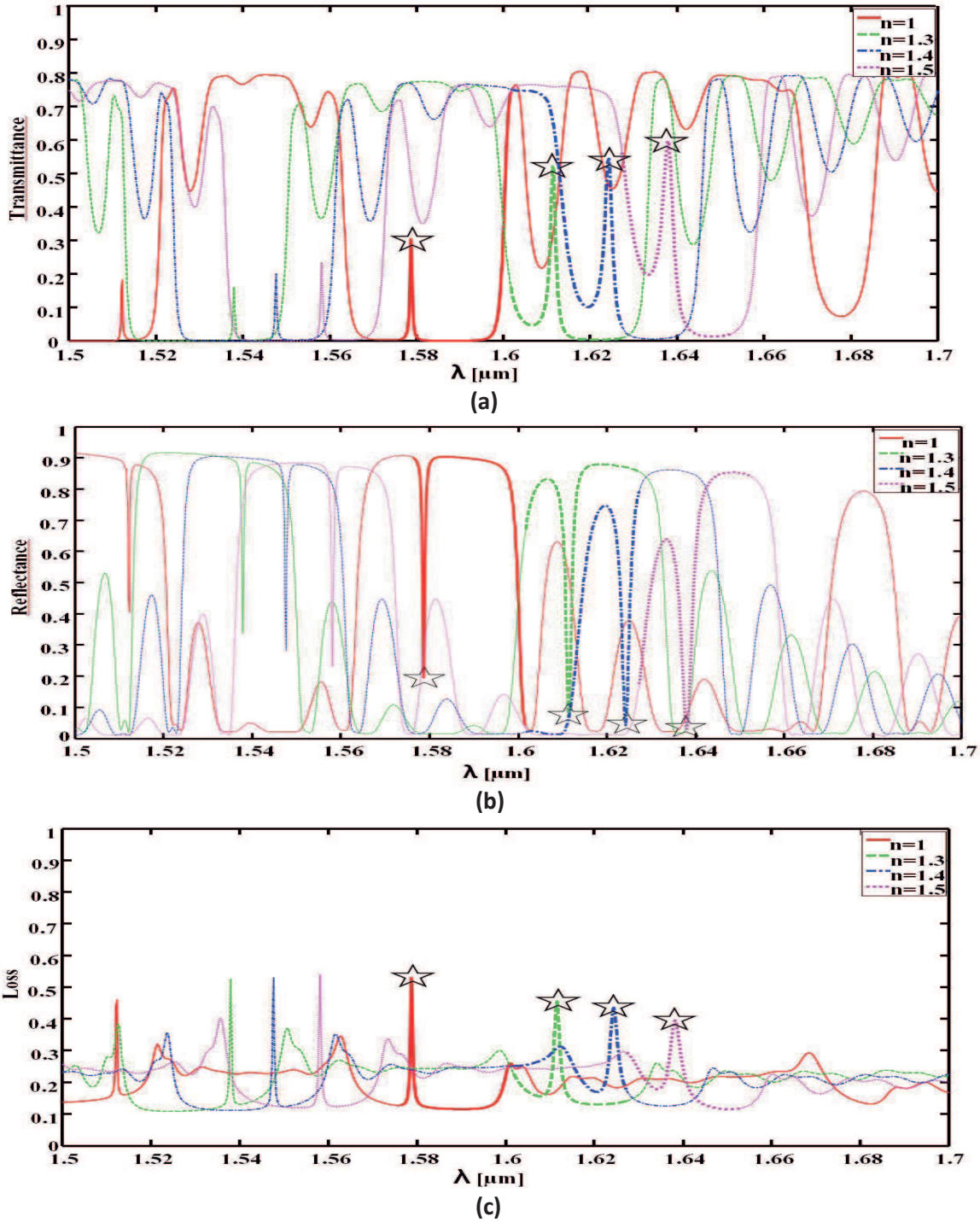


Fig. 2.5: (a) Transmittance, (b) reflectance, (c) out-of-plane loss spectrum (that is normalized to the input power and multiply by two) as a function of the wavelength, for $n$ = 1 (solid red line), 1.3 (dash green line), 1.4 (dash dot blue line) and 1.5 (dotted violet line), respectively, when the MPhC holes are filled by the analyte.

In order to evaluate the sensitivity ($S=\Delta\lambda/\Delta n$), Fig. 2.6 shows the position of the resonant wavelength as a function of the analyte refractive index. An analyte having refractive index *n* equal to 1, 1.3, 1.4 and 1.5 has been considered, when the MPhC holes are filled by the analyte. The evaluated sensitivity is 117 nm/RIU.

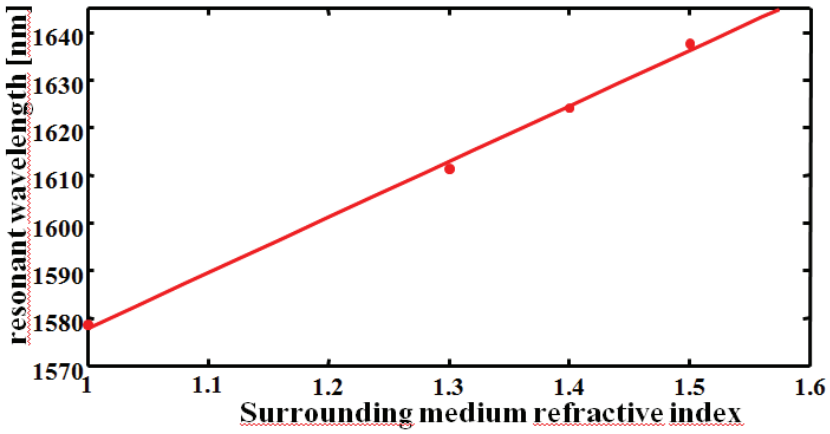


Fig. 2.6. Resonant wavelength as a function of the analyte refractive index (MPhC holes filled by the analyte).

## 2.3 *The experimental demonstration of a Mesoscopic Photonic Crystal 3D strip cavity*

A MPhC 3D Fabry-Pérot strip microcavity has been optimized and experimentally demonstrated, exhibiting high-Q and 3D-light confinement [90, 91]. The 3D design, fabrication and characterization are based on the collaboration among Politecnico di Bari, C2N CNRS of Université Paris-Sud and LAAS-CNRS of Toulouse.

In first approximation, the geometry of the single MPhC multilayer of Fig. 1.13 has been considered.

The MPhC 3D strip microcavity has the same geometrical and physical parameters of the structure described in Fig. 2.1 and is fully surrounded by air and has a thickness equal to 276 nm, a lattice constant $a$ equal to 350 nm, a hole radius $r = 0.25 \times a = 87.5$ nm, a bulk refractive index equal to $n_{GaAs} = 3.31$ (Fig. 2.7). The PMLs are imposed at the boundaries perpendicular to the $z$ direction, the central wavelength of the gaussian source is fixed (equal to 1550 nm) and the source band is in the range $1400nm < \lambda < 1700nm$.

Figure 2.8 shows the simulated spectrum of the vertically scattered light above the cavity (normalized to the input power) obtained by means of 3D-FDTD calculation (LUMERICAL). In good agreement with 2D-FDTD simulations reported in [47], despite the vertical losses, a long-lived mode showing a high-Q spectral peak around 1480 nm is observed with a Q-factor of about 4773 (≈ half of the corresponding 2D one). Another weaker peak, with a lower Q factor is also observed around 1551 nm (Q-factor equal to about 889).

In order to investigate the nature of both the modes, I have carried out a second set of 3D-FDTD simulations (LUMERICAL) where, in the xy-plane and in the xz-plane and at two resonant peaks, and the magnitude image and the profile graph of the electric field, the magnitude image and the profile graph of the Poynting vector, the absolute value image of the z-component of the Poynting vector have been obtained.

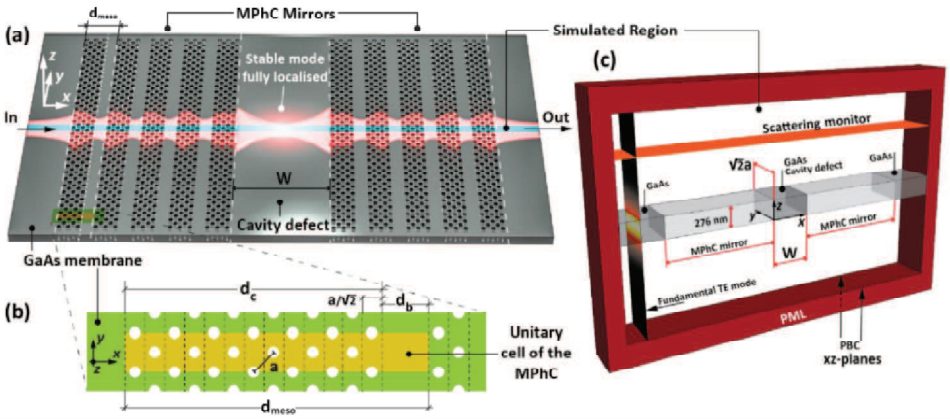


Fig. 2.7. (a) Sketch of the fabricated MPhC microcavity. The highlighted green and yellow area is reported in (b), where the yellow one represents the elementary cell of the MPhC. The highlighted light blue strip represents the portion of the structure that is actually designed and analysed in the 3D-FDTD simulation. (b) Sketch of the MPhC elementary cell. (c) Sketch of the FDTD calculation region. The red region, bordering the cell along the x- and z-directions, represent the PML boundary conditions. The two black vertical arrows indicate the xz-planes where the PBCs enclose the computational region along the y-direction. The orange strip, parallel to the xy-plane, represents the monitor where collect the scattered power is collected.

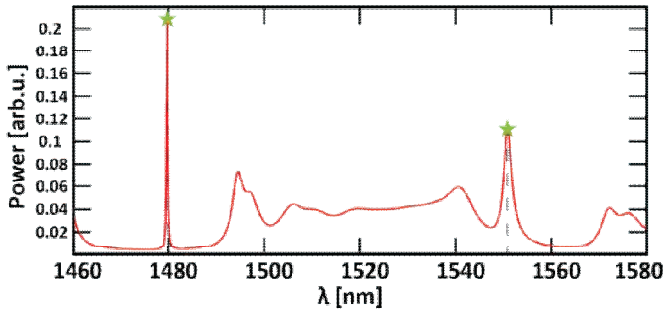


Fig. 2.8. 3D-FDTD vertically scattered light spectrum (normalized to the input power). The two peaks suggesting the formation of an optical mode inside the cavity are highlighted by two markers: one at 1480 nm and one at 1551 nm.

Figure 2.9 shows the self-normalized magnitude image of total electric field (linear scale) at 1480 nm (a) and at 1551 nm (b), and the self-normalized absolute value image of the z-component of the Poynting vector at 1480 nm (c) and 1551 nm (d). To highlight the vertically scattered light above the cavity, self-normalized Poynting vector depicted in Figures 2.9 (c)-(d) is plotted using a logarithmic scale. From these

simulations, we can conclude that both the spectral peaks correspond to modes that are fully localized: in xy-plane by the MSC cavity, and in the vertical direction by the membrane with partial leaking out of the membrane.

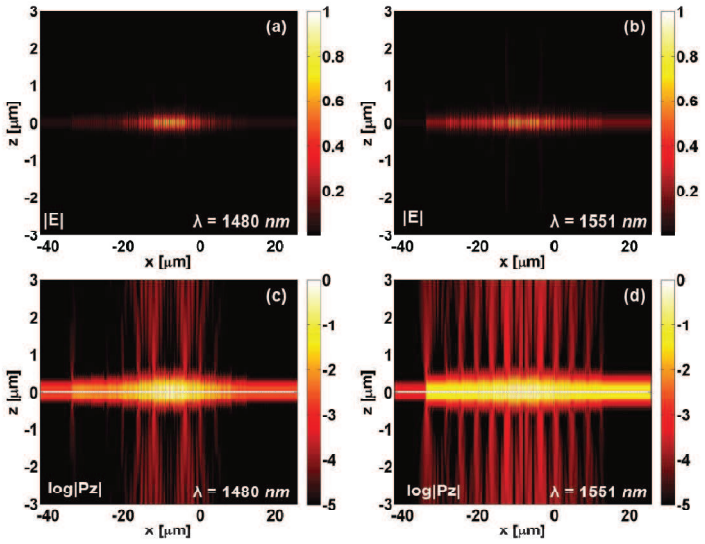


Fig. 2.9. Self-normalised magnitude of the total electric field in linear scale (a-b) and (c-d) self-normalised z-component of the Poynting vector in logarithmic scale at 1480 nm and 1551 nm, respectively.

At LAAS-CNRS of Toulouse several samples with the geometry described in Figure 2.7 were fabricated on suspended GaAs membranes in a three-step process described in [92]. Firstly, e-beam lithography was used to define the pattern in an electronic resist and form a mask that, in a second step, was used to etch the PhC holes using dry etching (ICP - RIE). In a last step, the samples were immersed into a hydrofluoric acid bath to remove a 1.5μm-thick AlGaAs sacrificial layer.

Fig. 2.10 (a, b) shows a scanning electron microscope (SEM) in-plane image of the micro-cavity (with an overall length along y and x of 92.5 μm and 41.3 μm, respectively).

At Politecnico di Bari the samples were optically characterized. Fig. 2.10 (c) shows the optical characterization set-up of the sample: the beam of a tunable laser (spanning 1460 – 1580 nm) is focused on the sample facet using two aspherical lenses; a polarizer,

placed in between the two lenses, controls the input light polarization. A microscope system, composed by a microscope objective and a VIS-IR vidicon camera, collects the scattered light and displays it on a monitor. Finally, the video signal is acquired by a commercial acquisition card and numerically processed.

An image of the scattered light is acquired for each wavelength, forming an hyperspectral cube $A(p_x,p_y,\lambda_p)$, where $\lambda_p$ is a given wavelength, $p_x$ and $p_y$ are the pixel indices along the x and y directions, respectively.

In Fig. 2.10 (a) the alignment position of the first and last row of the matrix of pixels ($p_x$=1 and $p_x$=$p_{x,cav}$ corresponding to the beginning and end of the cavity, respectively) are superimposed on the SEM image.

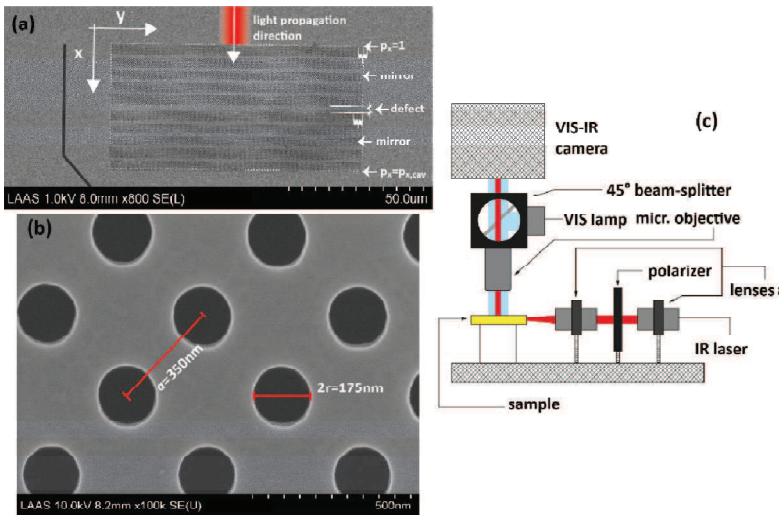


Fig. 2.10. (a) In-plane SEM image of a fabricated MPhC based microcavity having a lattice constant a=350 nm and a hole radius $r$=0.25×$a$=87.5 nm. The white arrows on the right indicate the position of the beginning and the end of the cavity and the defect position. The red stripe with a superimposed white arrow indicates the incident light direction. (b) Close-up of (a) inside a PhC slab. (c) Sketch of the optical characterization set-up of the sample.

In order to calculate the experimental vertically scattered light, we define a pseudospectral map $M(p_x,\lambda_p)$ as the sum of the pixel intensities $A$ along the transverse direction of the cavity (y-direction):

$$M(p_x,\lambda_p) = \sum_{p_y} A(p_x,p_y,\lambda_p). \quad (1.2)$$

The pseudospectral map $M(p_x,\lambda_p)$ allows to determine the following quantities:

$$S(\lambda_p) = \sum_{p_x=1}^{p_{x,cav}} M(p_x, \lambda_p) \tag{2.2}$$

$$N(\lambda_p) = \sum_{p_x=p_{x,cav}+1}^{p_{x,end}} M(p_x, \lambda_p) \tag{3.2}$$

$$\alpha = \frac{p_{x,cav}-1}{p_{x,end}-(p_{x,cav}+1)} \tag{4.2}$$

The useful signal is represented by $S(\lambda_p)$ that is the pseudospectral map integrated along the x-direction inside the cavity; the noise is represented by $N(\lambda_p)$ that is the pseudospectral map integrated along the x-direction outside of the cavity; α is a corrective coefficient that normalizes the cavity length with respect to the length of the noise region. Finally, the pseudospectrum $I(\lambda_p)$ is obtained as follows:

$$I(\lambda_p) = S(\lambda_p) - \alpha \cdot N(\lambda_p) \tag{5.2}$$

Fig. 2.11 (a) shows the experimental pseudospectral map of the fabricated microcavity in the wavelength range of interest. The final experimental vertically scattered light spectrum is evaluated by integrating the map along the x-axis.

Fig. 2.11 (b) shows the final experimental pseudospectrum (blue curve) that is compared with the simulated normalized vertically scattered light spectrum that I have calculated previously (red curve). This simulated spectrum is normalized to its maximum (as the pseudospectrum). The experimental results show a good agreement with the numerical ones. Specifically, in the experimental pseudospectrum the resonant peaks within the bandgaps, corresponding to the formation of a stable cavity mode, are at $\lambda_0$ = 1482.2 nm (green square mark) and $\lambda_3$ = 1547 nm (green star mark) allowing for a Q factor equal to 1720 and 1170, respectively. The differences between simulated and measured Q factors are attributed to the fact that the experimental beam is laterally confined, while in the simulation, an infinitely large beam was used.

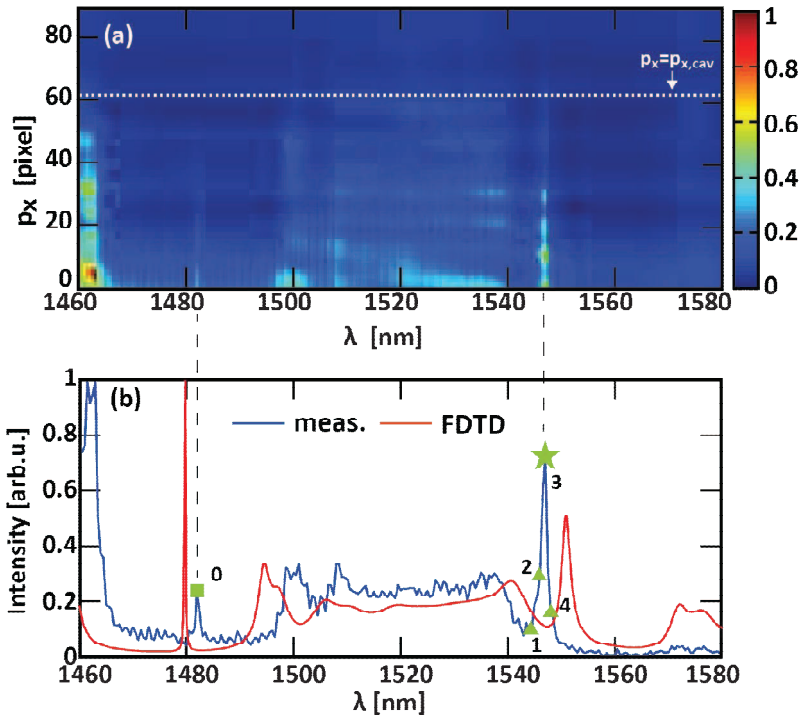


Fig. 2.11. (a) Measured pseudospectral map of the fabricated microcavity with $a$ = 350 nm. The superimposed horizontal white dotted line indicates the pixel labelled $p_{x,cav}$. (b) Experimental pseudospectrum (blue curve) and the simulated self-normalized scattering spectrum (red curve), which corresponds to the result shown on Figure 2.8. The green squared mark and the green star mark indicate the resonant peaks wavelengths $\lambda_0$ = 1482.2 nm and $\lambda_3$ = 1547 nm, respectively. The green triangle marks denote the wavelengths $\lambda_1$ = 1545 nm, $\lambda_2$ = 1546 nm and $\lambda_4$ = 1548 nm, corresponding to the subfigures shown in Fig 2.12.

To experimentally investigate the localization of the mode, we concentrate on the $\lambda_3$ = 1547 nm mode. We choose this mode as it exhibits a higher signal to noise ratio on the camera signal as compared to the $\lambda_0$ = 1482.2 nm mode. Figures 2.12 depicts the collected scattered light images at $\lambda_1$ = 1545 nm, $\lambda_2$ = 1546 nm, $\lambda_3$ = 1547 nm and $\lambda_4$ = 1548 nm. In particular, Fig. 2.12 (c) illustrates the formation of a stable mode at $\lambda_3$. At the same time, the region beyond the output facet in Figure 2.12 (c) is dark due to absence of scatterers (PhC holes and PhC/bulk interfaces).

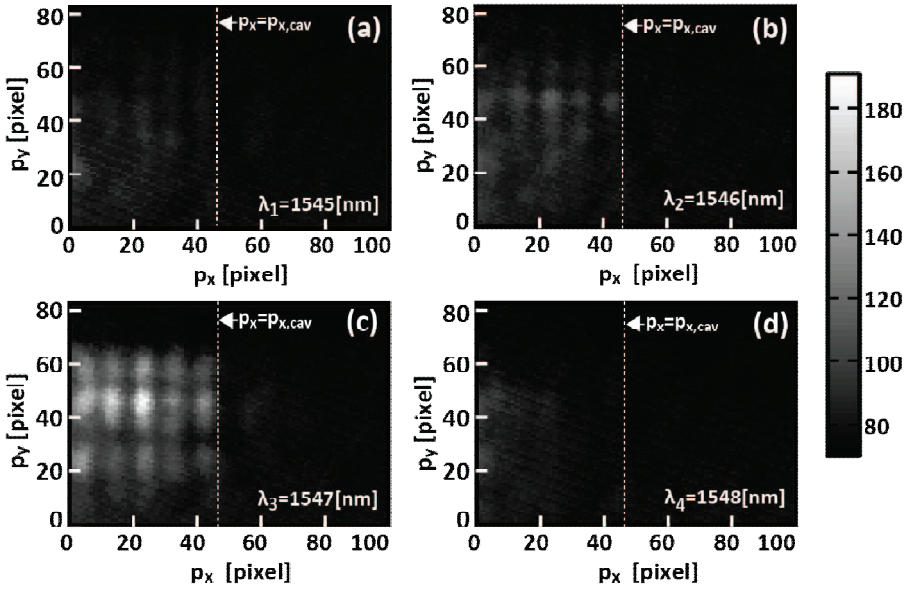


Fig. 2.12. Collected scattered light at wavelengths (a) $\lambda_1$, (b) $\lambda_2$, (c) $\lambda_3$ and (d) $\lambda_4$. The $p_y$-axis and the superimposed white dotted line indicate, respectively, the input facet ($p_x$= 1) and the output facet ($p_x$= $p_{x,cav}$) of the cavity, respectively.

## 2.4 *Mesoscopic Photonic Crystal 3D wide cavity devoted to optical trapping in air*

A high performance MPhC 3D wide microcavity for optical trapping of fine particulate matter in air has been designed and analysed, exhibiting high-Q and 3D-light confinement [93]. It has been numerically demonstrated the efficiency of the MPhC 3D wide microcavity for optical trapping in air: it is possible to obtain very high trapping potential for polystyrene particles having radii as small as 245 nm. The obtained results are extremely encouraging since it is possible to obtain extremely deep optomechanical potential well (about 4 times bigger than the minimum requirement for trapping) allowing for stable trapping, and opening the way for novel configurations for optical trapping of nano- and micro-particles, over areas of ~10×10 $\mu m^2$ in air, that could be linearly repositioned exploiting the translational invariance of the MPhC microcavity along the transverse direction.

In first approximation, the geometry of the single MPhC multilayer of Fig. 1.13 has been considered.

The MPhC 3D wide microcavity has the same geometrical and physical parameters of the structure described in Fig. 2.7 and has a length equal to 18 μm along the y-direction, the PMLs are imposed at the boundaries perpendicular to the *y* direction, the source is gaussian in the y-direction (Fig. 2.13).

I have carried out a numerical study on the influence of the source characteristics, evaluating the transmission, reflection and vertically scattered light spectra (normalized to the input power). I considered different values of the gaussian source waist radius ($w_0$ = 7.5 ×a/2, 15×a/2, 20×a/2).

Figures (2.14a) and (2.14b) show, respectively, the simulated transmission and reflection spectra, normalized to the input power, when the source waist radius is fixed equal to 20×a/2. The wavelength resolution in the range 1460-1580nm is equal to 0.2 nm. When MMs composed by only 5 superperiods are considered, a long-lived mode showing a high-Q spectral peak around 1484 nm is observed with a Q-factor of about 3709. Another peak, with a lower Q-factor, is also observed around 1554 nm (Q-factor equal to about 706). By decreasing the source waist radius $w_0$ down to 7.5 ×a/2, the

spectral position of the peaks remains unchanged while the Q-factor of both spectral peaks decreases, reaching the values 2473 and 409 for the peaks at λ= 1484 and 1554 nm, respectively. Higher Q-factors are expected for MMs composed by a larger number of superperiods.

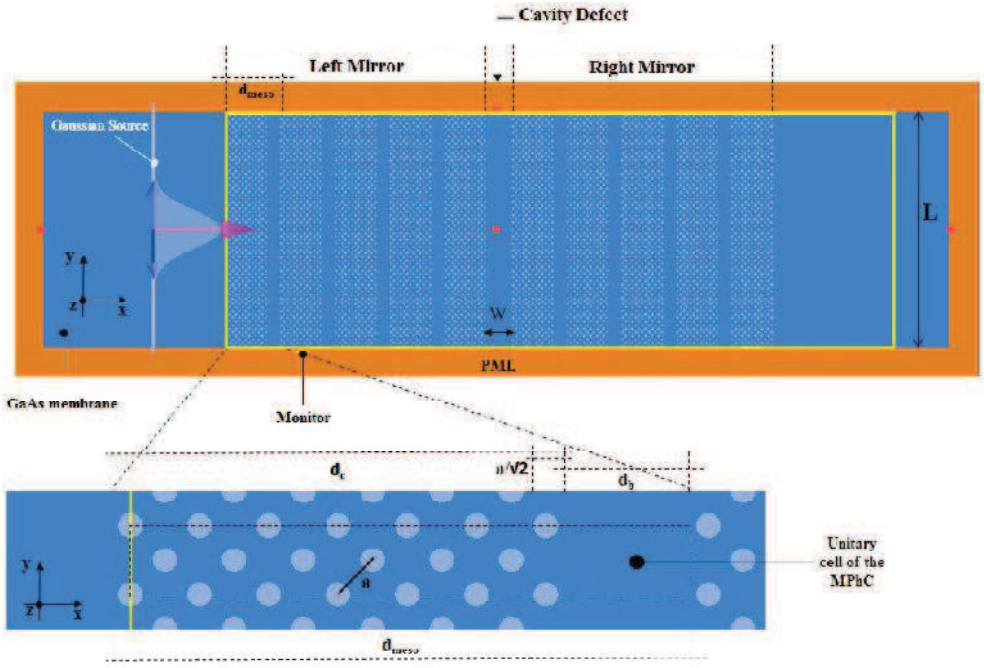


Fig. 2.13. (Top) Sketch of the MPhC microcavity simulated by means of the 3D-FDTD method. (Bottom) The highlighted area represents the elementary cell of the MPhC. The orange region, overlapping the cell along the x- and y-directions, represents the PML boundary conditions. The yellow region, parallel to the xy-plane, represents the monitor where the total electric field is collected.

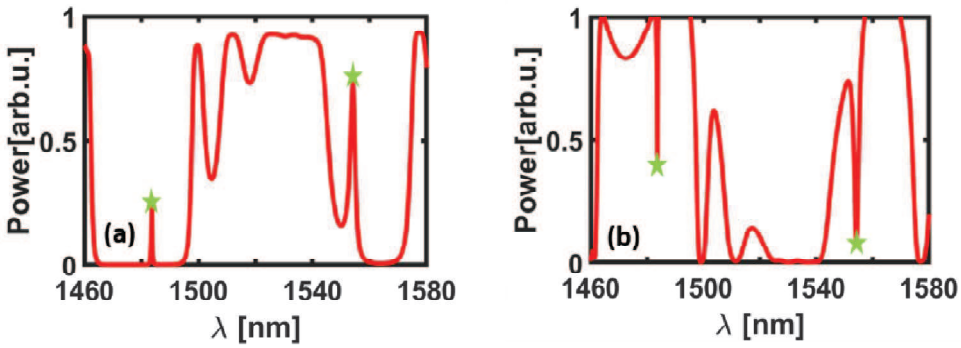


Fig. 2.14. 3D-FDTD (a) transmittance and (b) reflectance spectra: the two peaks, suggesting the formation of an optical mode inside the cavity, are highlighted by two markers: the former at 1484 nm and the latter at 1554 nm. Source waist radius $w_0 = 20 \times a/2$.

In order to investigate the nature of both the modes, the in-plane total electric field on the top of the membrane and at two resonant peaks, considering different values of the gaussian source waist radius ($w_0$ = 7.5 ×a/2, 20×a/2) has been evaluated.

Figure 2.15 shows the self-normalized magnitude of the electric field (linear scale) at 1484 nm (a) and at 1554 nm (b), considering the source waist radius $w_0$ = 20×a/2. Both the spectral peaks correspond to modes that are fully localized in xy-plane by the MSC cavity while partial leaking out of the membrane has been observed in the vertical direction (z-axis). It is worth noting that the MSC cavity provides 2D confinement in the xy-plane despite being essentially translationally invariant along the transverse direction y. The cavity can be arbitrarily extended along the y direction without modifying the in-plane confinement. Moreover, the excitation beam and, in turn, the confined optical mode can be freely moved along the y direction, allowing one degree of freedom.

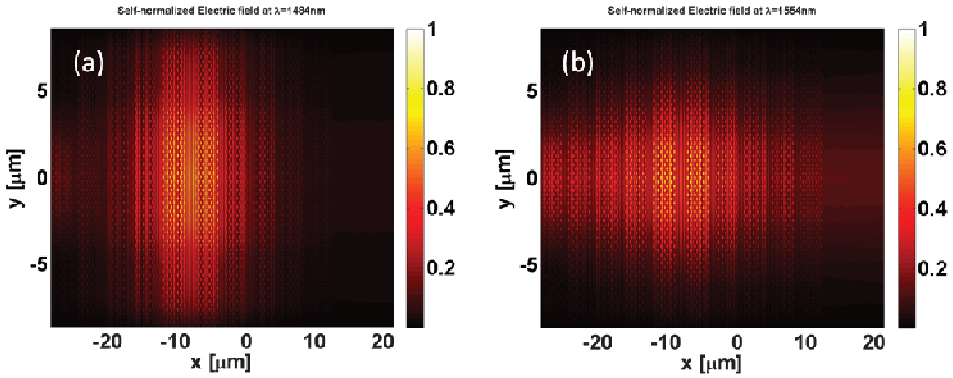


Fig. 2.15. Close-up of the self-normalised magnitude of the total in-plane electric field at (a) 1484 nm and (b) 1554 nm, respectively, considering the source waist radius $w_0$ = 20×a/2.

Moreover I have performed the analysis, finalized to the optical trapping evaluation, of the MPhC 3D wide microcavity by means of 3D-FDTD simulations (LUMERICAL), evaluating the total electric field in the air volume at the top of the structure at two resonant peaks in absence of the bead to be trapped, considering $w_0$ = 20×a/2. The 3D region, where I have retrieved the field, has dimensions equal to 50 μm along the x direction, 18 μm along the y direction and 0.5 μm along the z direction.

Based on these last results considering the waist radius $w_0 = 20\times a/2$, to evaluate the optical trapping two approaches have been considered: the former is based on computing the optomechanical trapping potential by means of the gradient force density convolution method (Matlab) and the latter is based on the calculation of the total optomechanical force by means of Maxwell stress tensor-based method (Lumerical).

In particular, the total optomechanical force acting on an object, that interacts with an arbitrary electromagnetic field, arises from the light-matter momentum exchange occurring during the interaction. This force can be considered as the superposition of two terms:

(i) a reactive term, the so-called gradient force $F_g$, which is conservative and arises from field intensity gradients;

(ii) a dissipative one, known as scattering force, that takes into account the non-conservative interactions, such as the momentum transfer due to field scattering and the radiation pressure [71].

These two contributions can be rigorously separated for very small particles ($d \ll \lambda$) and become increasingly intertwined as the fields become rapidly varying in the spatial region occupied by the object. However, it has been shown in [71, 72, 94], that, in presence of a strong near field and when the Poynting vectors cancels out (as it happens within the defect of a cavity due to the establishment of steady waves), the gradient term can be a good approximation of the total force. This can be calculated as follows:

$$F_g(r) = -\nabla\left(-\frac{\varepsilon_0}{4}\alpha\iiint_{Bead}\left|E_0(s)\right|^2 dV\right) = -\nabla U \tag{6.2}$$

where $\varepsilon_0$ is the void permittivity, $\alpha$ is the object polarizability, and $E_0$ the total electric field that I have retrieved by means of 3D-FDTD calculations in absence of the bead to be trapped.

Thus, the trapping potential U can be seen as the convolution integral between the square modulus of the aforementioned electric field $E_0$ and a masking function M being unitary inside the bead volume and zero outside:

$$U(r) = -\frac{\varepsilon_0}{4}\alpha \iiint \left|E_0(s)\right|^2 M(r-s)dV_s = (u * M)(r) \tag{7.2}$$

where u represents the energy density function. It has been considered a polystyrene bead (n=1.59) having radii of 50, 100, 245 nm, when an injected power of 10 mW is considered.

Results below reported are calculated considering the center of the cavity defect and a distance from the top of the structure equal to the bead diameter [93].

Figure 2.16 shows the optomechanical potential, normalized to the thermal energy ($U/k_bT$), corresponding to the spectral peak $\lambda$ =1484 nm (having higher Q-factor), when the bead radius is r = 50 nm (Fig. 2.16 a-b), r = 100 nm (Fig. 2.16 c-d), r = 245 nm (Fig. 2.16 e-f). As we can infer from the figure, by increasing the bead radius the trapping potential increases. At its minima, the potential well is deeper than -38 for the case r = 245 nm (Fig. 2.16 e-f), while for r = 100 nm (Fig. 2.16 c-d) its depth is beyond -10. For the third case (higher radius), trapping potential is considerably deep, about 4 times bigger than the minimum (equal to -10) required for trapping by the criterion proposed by Ashkin et al. in [78].

Figure 2.17 shows the optomechanical potential, normalized to the thermal energy ($U/k_bT$), corresponding to the spectral peak (a) $\lambda$ =1484 nm and (b) $\lambda$ =1554 nm, respectively, when the bead radius is 245 nm. Figure 2.17 (a) clearly shows that the trapping potential is very deep over an area of about 10×10 $\mu m^2$ around the cavity defect. This may be also suitable for multiple object trapping.

Finally, in Figure 2.18 we show a map of the optomechanical potential, normalized to the thermal energy ($U/k_bT$), corresponding to the spectral peak $\lambda$ =1484 nm when the bead radius is 245 nm, as a function of the input power $P_{in}$ [mW] and the temperature T [K]. The dashed white line represents the "threshold" of the minimum trapping potential (equal to - 10) while the dashed black line corresponds to the room temperature. Halving the input power value, the optomechanical potential decreases while maintaining still interesting values for trapping. This map clearly shows that trapping

potential exceeds the "threshold" over a large range of both input power and temperature.

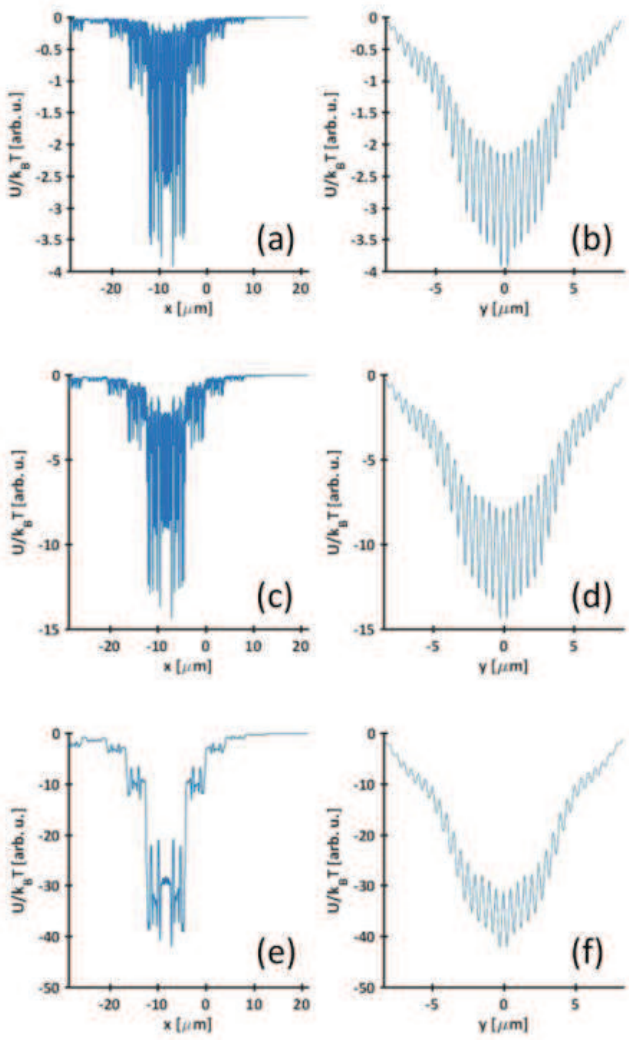


Fig. 2.16. Optomechanical potential at room temperature along (a-c-e) the x-axis, for y=0, and (b-d-f) y-axis, for x= -8.27μm, respectively, normalized to the thermal energy ($U/k_bT$), corresponding to the spectral peak $\lambda$ =1484 nm, when the bead radius is (a-b) r = 50 nm, for z=100nm, (c-d) r = 100 nm, for z=200nm, (e-f) r = 245 nm, for z=320nm, respectively, and $w_0 = 20 \times a/2$.

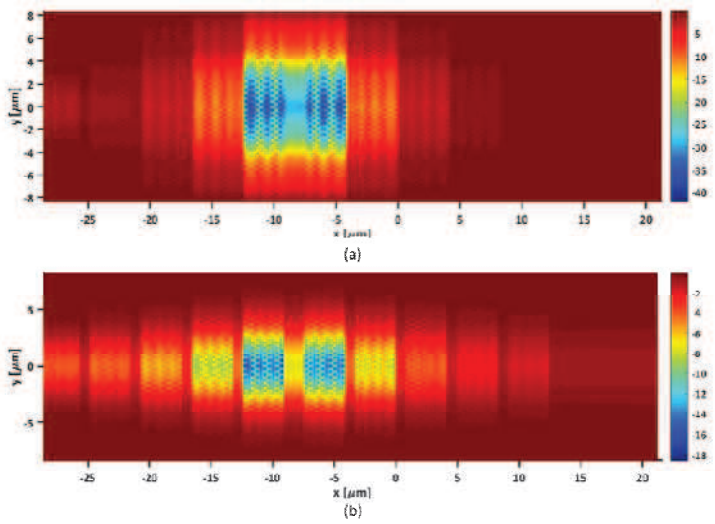


Fig. 2.17. Optomechanical potential at room temperature, normalized to the thermal energy ($U/k_bT$), corresponding to the spectral peak (a) $\lambda$ =1484 *nm* and (b) $\lambda$ =1554 *nm*, respectively, when the bead radius is 245 *nm*, for z=320nm, and $w_0 = 20 \times a/2$.

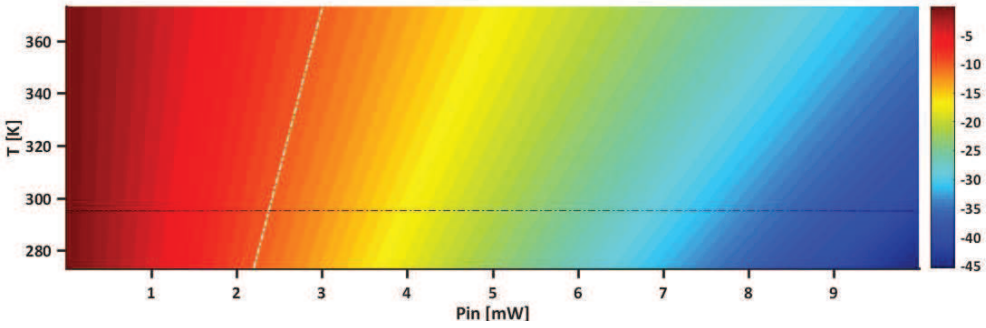


Fig. 2.18. Optomechanical potential, normalized to the thermal energy ($U/k_bT$), corresponding to the spectral peak $\lambda$ =1484 nm when the bead radius is 245 nm, for x= -8.27μm, y=0 and z=320nm, and $w_0 = 20 \times a/2$, as a function of the input power $P_{in}$ and the temperature T.

Further optical trapping evaluation regards the calculation of total optomechanical force by means of Maxwell stress tensor-based method in presence of the bead to be trapped [93]. The total force is constituted by both the gradient force and the scattering force, which takes into account the non-conservative interactions such as the momentum transfer due to field scattering and the radiation pressure. It has been always considered a polystyrene bead (n=1.59), that has radii of 250, 500 nm, placed at a distance from the

top of the structure equal to 2 nm and localized in the center of the cavity defect. In the numerical analysis the Maxwell stress tensor-based calculation computes the Maxwell Stress Tensors over the faces of a closed box, that surrounds only the bead, and then integrates them over the closed surface. The graph of the total force as a function of wavelength by means of LUMERICAL confirms the trapping: at the spectral peak $\lambda$ =1484 nm the bead undergoes a strong pulling force (directed toward the membrane surface) with values equal to 1233 pN/W (r=250 nm) and 2874 pN/W (r=500 nm) which are comparable to those observed in plasmonic tweezers [71].

## 2.5 *Mesoscopic Photonic Crystal 3D wide cavity devoted to optical trapping in water*

As for the case of optical trapping in air of the previous paragraph 2.4, an optical trapping device in water based on a MPhC 3D wide microcavity has been designed and analysed. In this case it has been possible to obtain very high trapping potential for polystyrene particles having radii as small as 200 nm. The obtained results are extremely encouraging since it is possible to obtain extremely deep optomechanical potential well (about 5 times bigger than the minimum requirement for trapping) allowing for stable bio-trapping, and opening the way for novel configurations for optical bio-trapping of nano- and micro-particles, over areas of ~10×10 $\mu m^2$ in water, that could be linearly repositioned exploiting the translational invariance of the MPhC microcavity along the transverse direction.

The design of the geometry of the single MPhC multilayer is performed by means of the 3D plane wave expansion method (3D-MPB), described in Fig. 1.14.

The MPhC 3D wide microcavity has the same geometrical and physical parameters of the structure described in Fig. 2.13 and has a thickness equal to 250 nm and it is fully surrounded by water (the MPhC holes are filled by water) that has refractive index n=1.33, a bulk refractive index equal to $n_{GaAs}$ = 3.355, a bulk width $d_b$ = 16.9992×$a$, the central wavelength of the gaussian source is equal to 1421 nm and the source band is equal to $1271nm < \lambda < 1571nm$.

For this structure, considering the gaussian source waist radius $w_0$ = 20×a/2, I have obtained the transmission (normalized to the input power) (Fig. 2.19). A long-lived mode showing a spectral peak around 1431 nm is observed with a Q-factor of about 2385. Another peak, with a higher Q-factor, is also observed around 1492 nm (Q-factor equal to about 2486).

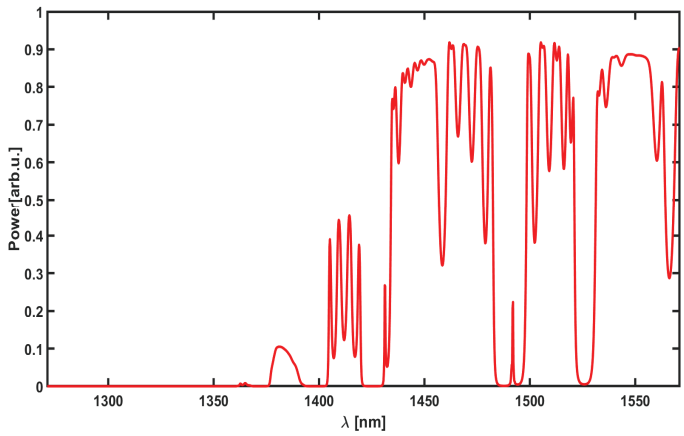


Fig. 2.19. 3D-FDTD transmittance spectra: the two peaks, suggesting the formation of an optical mode inside the cavity, are: the former at 1431 nm and the latter at 1492 nm. Source waist radius $w_0 = 20\times a/2$.

In order to investigate the nature of the higher Q-factor mode, the in-plane total electric field on the top of the membrane and at resonant peak 1492 nm, considering the gaussian source waist radius $w_0 = 20\times a/2$ has been evaluated. Fig. 2.20 shows the self-normalized magnitude image of the electric field (linear scale). The spectral peak corresponds to a mode that is fully localized in xy-plane by the MSC cavity.

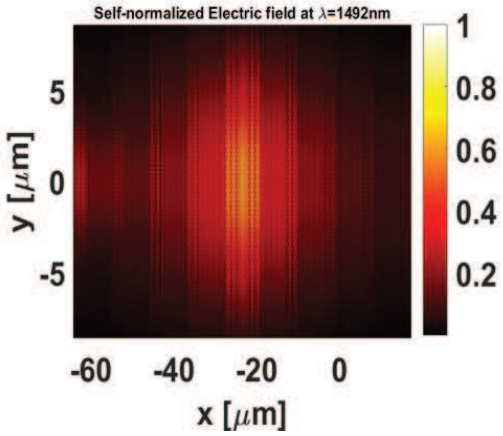


Fig. 2.20. Close-up of the self-normalised magnitude of the total in-plane electric field at 1492 nm, considering the source waist radius $w_0 = 20\times a/2$.

Moreover I have performed the analysis, finalized to the optical trapping evaluation, of the MPhC 3D wide microcavity, evaluating the total electric field in the water volume

at the top of the structure at resonant peak 1492 nm (having higher Q-factor) in absence of the bead to be trapped, considering the gaussian source waist radius $w_0 = 20\times a/2$. The 3D region, where I have retrieved the field, has dimensions equal to 81 μm along the x direction, 18 μm along the y direction and 0.5 μm along the z direction.

Considering the waist radius $w_0 = 20\times a/2$, the optical trapping has been evaluated computing the optomechanical trapping potential by means of the gradient force density convolution method (Matlab), described in Eq. (6.2) and in Eq. (7.2). It has been considered a polystyrene bead (n=1.59) having radii of 50, 100, 200, 245 nm, when an injected power of 10, 50, 100 mW is considered.

Results below reported are calculated considering the center of the cavity defect and a distance from the top of the structure equal to the bead diameter.

Figure 2.21 shows the optomechanical potential, normalized to the thermal energy ($U/k_bT$), corresponding to the spectral peak $\lambda$ =1492 nm (having higher Q-factor) and to an injected power of 50 mW, when the bead radius is r = 50 nm (Fig. 2.21 a-b), r = 100 nm (Fig. 2.21 c-d), r = 200 nm (Fig. 2.21 e-f). As we can infer from the figure, by increasing the bead radius the trapping potential increases. At its minima, the potential well is deeper than -50 for the case r = 200 nm (Fig. 2.21 e-f), while for r = 100 nm (Fig. 2.21 c-d) its depth is beyond -10. For the third case (higher radius), trapping potential is considerably deep, about 5 times bigger than the minimum (equal to -10) required for trapping by the criterion proposed by Ashkin et al. in [78]. Compared to the previous paragraph 2.4 to obtain a very deep potential, that is 5 times bigger than the minimum (equal to -10) required for trapping, it has to be always considered the higher radius and moreover it has to be supposed a higher injected power that is 50 mW.

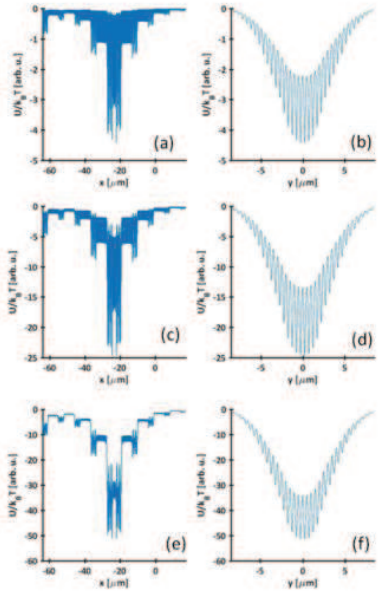


Fig. 2.21. Optomechanical potential at room temperature along (a-c-e) the x-axis, for y=0, and (b-d-f) y-axis, for x= -23.4μm, respectively, normalized to the thermal energy ($U/k_bT$), corresponding to the spectral peak λ =1492 nm and to an injected power of 50 mW, when the bead radius is (a-b) r = 50 nm, for z=100nm, (c-d) r = 100 nm, for z=200nm, (e-f) r = 200 nm, for z=280nm, respectively, and $w_0 = 20 \times a/2$.

Figure 2.22 shows the optomechanical potential, normalized to the thermal energy ($U/k_bT$), corresponding to the spectral peak λ =1492 nm, when the bead radius is 200 nm and an injected power of 50 mW is considered (that is higher than that of the previous paragraph 2.4). Figure 2.22 clearly shows that the trapping potential is very deep over an area of about 10×10 $\mu m^2$ around the cavity defect. This may be also suitable for multiple object trapping.

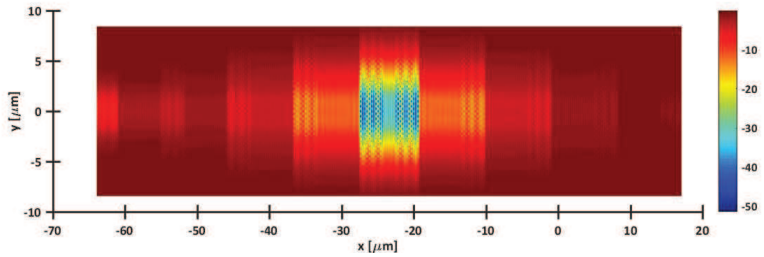


Fig. 2.22. Optomechanical potential at room temperature, normalized to the thermal energy ($U/k_bT$), corresponding to the spectral peak λ =1492 *nm*, when the bead radius is 200 *nm*, for z=280nm, and an injected power of 50 mW is considered and $w_0 = 20 \times a/2$.

Finally, in Figure 2.23 we show a map of the optomechanical potential, normalized to the thermal energy ($U/k_bT$), corresponding to the spectral peak $\lambda$ =1492 nm when the bead radius is 200 nm and an injected power of 50 mW is considered (that is higher than that of the previous paragraph 2.4), as a function of the input power $P_{in}$ [mW] and the temperature T [K]. The dashed white line represents the "threshold" of the minimum trapping potential (equal to - 10) while the dashed black line corresponds to the room temperature. Halving the input power value, the optomechanical potential decreases while maintaining still interesting values for trapping. This map clearly shows that trapping potential exceeds the "threshold" over a large range of both input power and temperature.

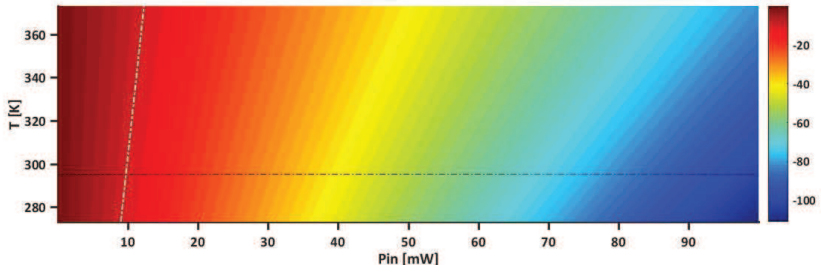


Fig. 2.23. Optomechanical potential, normalized to the thermal energy ($U/k_bT$), corresponding to the spectral peak $\lambda$ =1492 nm when the bead radius is 200 nm, for x= -23.4μm, y=0 and z=280nm, and an injected power of 50 mW is considered and $w_0 = 20 \times a/2$, as a function of the input power $P_{in}$ and the temperature T.

Following, for this structure I have carried out a numerical study on the influence of the cavity defect characteristics, evaluating the transmission spectrum (normalized to the input power). I considered different values of the cavity defect length in the x-direction ($L_d$ = 5.266 ×a, 5.373×a), lower and higher than the current cavity defect length ($L_d$ = 5.32 ×a), respectively. It has been observed that the spectral position of the two peaks remains almost unchanged, while the Q-factors of both spectral peaks increase or remain almost unchanged. In particular, by decreasing the cavity defect length $L_d$ down to 5.266 ×a a long-lived mode showing a high-Q spectral peak around 1430 nm is observed with a Q-factor of about 3576. Another peak, with a lower Q-factor, is also observed around 1490 nm (Q-factor equal to about 2484). By increasing the cavity

defect length $L_d$ up to 5.373 ×a, the Q-factor reaches the values 2386 and 3733 for the peaks at λ= 1432 and 1493 nm, respectively. Therefore, this last case ($L_d$ = 5.373×a) allows to obtain the higher Q-factor (Q=3733 at λ=1493 nm), and then it will allow to obtain the aforementioned very deep optomechanical potential exploiting an injected power lower than 50 mW.

Figure 2.24 shows the simulated transmission spectrum, normalized to the input power, when the cavity defect length $L_d$ is fixed equal to 5.373 ×a.

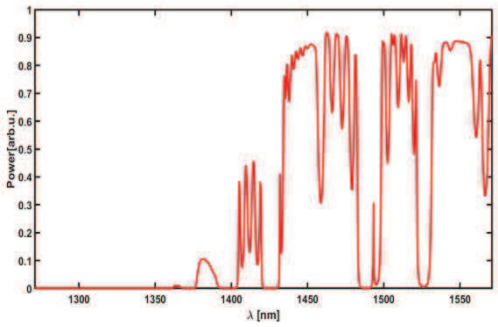


Fig. 2.24. 3D-FDTD transmittance spectrum: the two peaks, suggesting the formation of an optical mode inside the cavity, are: the former at 1432 nm and the latter at 1493 nm. Source waist radius $w_0$ = 20×a/2 and cavity defect length $L_d$=5.373 ×a.

In order to investigate the nature of the higher Q-factor mode, the in-plane total electric field on the top of the membrane and at resonant peak 1493 nm, considering the cavity defect length $L_d$ = 5.373×a has been evaluated. Fig. 2.25 shows the self-normalized magnitude image of the electric field (linear scale). The spectral peak corresponds to a mode that is fully localized in xy-plane by the MSC cavity.

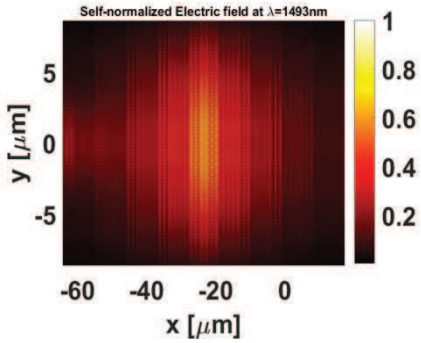


Fig. 2.25. Close-up of the self-normalised magnitude of the total in-plane electric field at 1493 nm, considering the source waist radius $w_0$ = 20×a/2 and the cavity defect length $L_d$=5.373 ×a.

Moreover I have performed the analysis, finalized to the optical trapping evaluation, of the MPhC 3D wide microcavity, evaluating the total electric field in the water volume at the top of the structure at resonant peak 1493 nm (having higher Q-factor) in absence of the bead to be trapped, considering the cavity defect length $L_d = 5.373 \times a$.

Considering the cavity defect length $L_d = 5.373 \times a$, the optical trapping will be evaluated, as for the aforementioned structure having $L_d = 5.32 \times a$, computing the optomechanical trapping potential by means of the gradient force density convolution method (Matlab). The aforementioned very deep optomechanical potential will be obtained exploiting an injected power lower than 50 mW.

# 3. MESOSCOPIC PHOTONIC CRYSTAL WAVEGUIDES

## 3.1 *Mesoscopic Photonic Crystal 3D strip and 3D wide waveguides devoted to routing element*

High performance MPhC 3D strip and 3D wide waveguides have been designed and analysed, exhibiting high transmission, strong mesoscopic self-collimation, translational invariance, and the unwanted reflections at PhC input interfaces are minimal, without either affecting the feasibility or the complexity of the structure [96].

In first approximation, the design of the geometry of the single MPhC multilayer was performed by means of the 2D plane wave expansion method (2D-MPB), described in Fig. 1.13.

Fig. 3.1 shows the MPhC 3D waveguide that is 13-mesoperiod-long along the x-direction. The whole device is etched on a 270 *nm*-thick membrane of GaAs ($n_{GaAs}$ = 3.4), fully surrounded by air. Each mesoperiod is obtained by interleaving focusing slabs constituted by 5 hole rows of a 45°-tilted hole-type square-lattice PhC (having lattice constant $a$ = 360 nm, hole radius $r = 0.28\times a$ and an overall width $d_c = 3.536\times a$), and defocusing slabs constituted by bulk material having a refractive index $n_{GaAs}$ and a width $d_b = 0.747\times a$.

The periodic structure, showing a period $\sqrt{2}\times a$, has a length along the y-direction: a) in the 3D strip waveguide configuration, 0.51 μm (equivalent to 3 PhC hole rows) and b) in the 3D wide waveguide configuration, 40 μm (equivalent to 172 PhC hole rows).

Perfectly matched layers (PMLs) were imposed at the boundaries of the 3D computational cell along the three directions, but, in the 3D strip waveguide, periodic boundary conditions (PBCs) were imposed at the 3D computational cell boundaries perpendicular to y-direction.

The structure was excited by injecting a gaussian source (1400 nm < λ < 1700 nm) having a spatial distribution matching that of the fundamental TE mode (with the x-component of the electric field $E_x = 0$) of the membrane (at λ = 1550 nm).

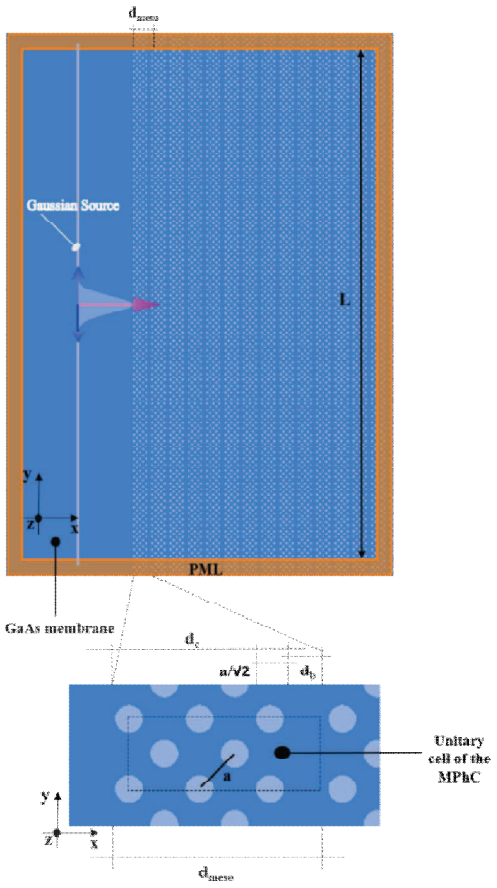


Fig. 3.1. (Top) Sketch of the MPhC waveguide simulated by means of the 3D-FDTD method. The orange region represents the PML boundary conditions. (Bottom) The highlighted area represents the elementary cell of the MPhC.

For the MPhC 3D wide waveguide, considering a gaussian source along the y-direction with waist radius $w_0 = 10 \times a/2$, the transmission, reflection, out-of-plane loss and lateral loss spectra (normalized to the input power) have been obtained. These spectra have been compared with the respective spectra of the MPhC 3D strip waveguide obtained considering a constant source along the y-direction (Fig. 3.2).

The transmittance spectrum exhibits several peaks with almost 80 % transmission near the central source wavelength $\lambda_0$=1550 nm. However, the optimal performance is achieved for a wavelength $\lambda_1$=1591 nm in the MPhC 3D wide waveguide and $\lambda_2$=1500 nm in the MPhC 3D strip waveguide (black dashed lines), slightly above and under $\lambda_0$, respectively, with almost 83 % and 85 % transmission, respectively.

A mini bandgap opens around λ=1508 nm, corresponding to the dip appearing in Fig. 3.2. This is due to the overall mesoscopic-periodicity and shows a low transmission of about 60 % with a slight refocusing of the beam.

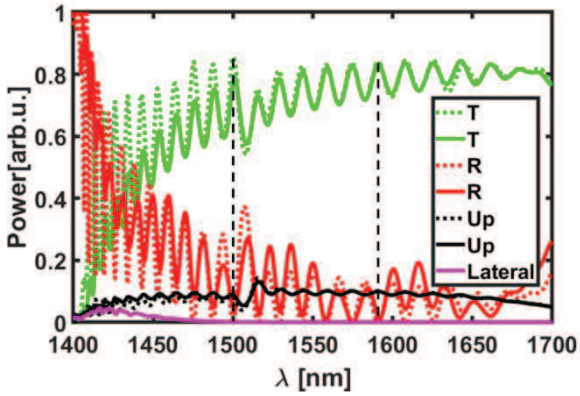


Fig. 3.2. Transmittance (T), reflectance (R), out-of-plane loss (Up) and lateral loss (Lateral) spectra, considering the MPhC 3D wide waveguide (solid lines) and the MPhC 3D strip waveguide (dot lines).

In order to investigate the mesoscopic self-collimation and the out-of-plane loss, another set of 3D-FDTD simulations has been carried out where the total Poynting vector has been recorded in the xy-plane and in the xz-plane and at the optimised wavelength 1591 nm, considering the MPhC 3D wide waveguide.

Fig. 3.3 shows the self-normalized magnitude of the Poynting vector at the optimised wavelength 1591 nm (linear scale) in xy-plane, considering the MPhC 3D wide waveguide. The MPhC 3D wide waveguide shows a negligible reflection at the input interface (x=-9.84 μm) and a collimated beam over the whole structure.

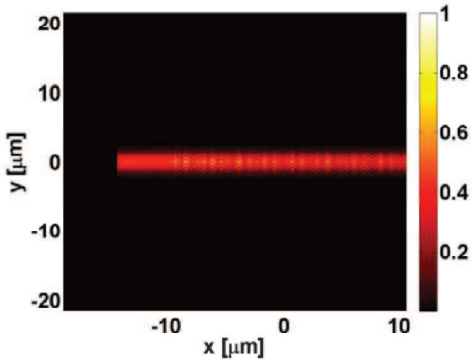


Fig. 3.3. Self-normalized magnitude of the Poynting vector at 1591 nm (linear scale), considering the MPhC 3D wide waveguide.

Fig. 3.4 shows the self-normalized magnitude of the Poynting vector at 1591 nm in logarithmic scale in the xz-plane, considering the MPhC 3D wide waveguide, and puts in evidence the out-of-plane losses (17%).

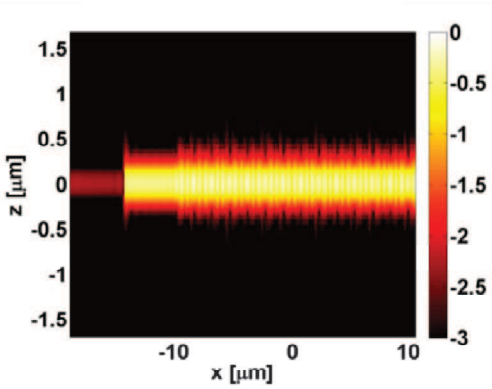


Fig. 3.4. Self-normalized magnitude of the Poynting vector at 1591 nm (logarithmic scale), considering the MPhC 3D wide waveguide.

These results open the way for developing a full class of routing elements that can be combined together, a cascadable circuitry out of these building blocks, and a circuitry taking advantage of the spatial and spectral reconfigurability that this MSC offers. Fig. 3.5 shows that the routing elements (spatial reconfigurability) and the wavelength splitters (spectral reconfigurability) could be obtained by interleaving different mesoperiods, that have different PhC slabs widths and different bulk slabs widths.

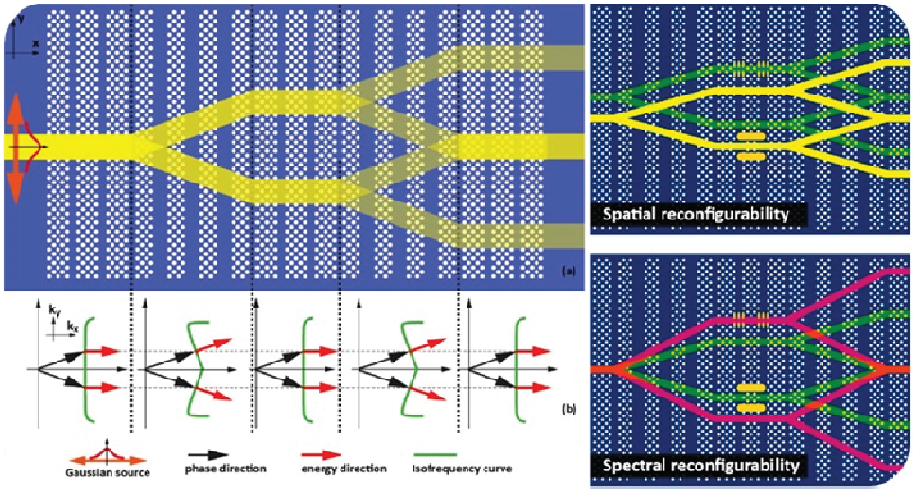


Fig. 3.5. Operation of the mesoscopic routing element.

## 3.2 *Mesoscopic Photonic Crystal 3D wide waveguide: the influence of the gaussian source waist on the collimation phenomenon*

The influence of the characteristics of the gaussian source on the collimation phenomenon in a MPhC 3D wide waveguide has been explored by considering different values of the waist radius [97]. The optimum value of the source waist radius $w_o$ has to guarantee that the MPhC 3D wide waveguide exhibits: i) minimal unwanted reflections at PhC input interfaces without either affecting the feasibility or the complexity of the structure, ii) high transmission, iii) strong mesoscopic self-collimation and iv) translational invariance.

In this case the 3D geometrical parameters of the single MPhC multilayer have been fixed by considering the map in Fig. 1.15.

The MPhC 3D wide waveguide has the same geometrical and physical parameters of the structure described in Fig. 3.1 and has a bulk width $d_b = 3.1048 \times a$, the central wavelength of the gaussian source is equal to 1520 nm and the source band is equal to $1370nm < \lambda < 1670nm$ (Fig. 3.6).

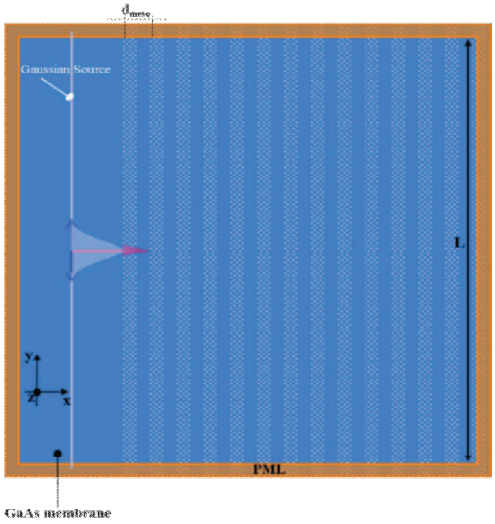


Fig. 3.6. Sketch of the mesoscopic photonic crystal 3D wide waveguide.

For this structure, the transmission, reflection, out-of-plane loss and lateral loss spectra (normalized to the input power) have been evaluated. Different values of the gaussian source waist radius have been considered.

For example for the source waist radius $w_o$ equal to 15a/2, Fig. 3.7 shows that the transmittance spectrum exhibits several peaks with almost 66% transmission near the central source wavelength $\lambda_0$=1520nm (black dashed line). However, the optimal performance is achieved for a wavelength $\lambda_1$=1567nm with almost 85% transmission (black dashed line), slightly above $\lambda_0$.

A mini bandgap opens around $\lambda$=1545nm, corresponding to the dip appearing in Fig. 3.7. This is due to the overall mesoscopic-periodicity and shows a low transmission of about 5% with a slight refocusing of the beam.

When the source waist radius $w_o$ is assumed equal to 10a/2, the transmittance spectrum exhibits several peaks with almost 62% transmission near the $\lambda_0$ and the optimal performance is achieved for a wavelength $\lambda_1$=1587nm with almost 83% transmission.

As for the case $w_o$=15a/2, also in this last case a mini bandgap opens around $\lambda$=1545nm showing a transmission of about 5% with a slight refocusing of the beam.

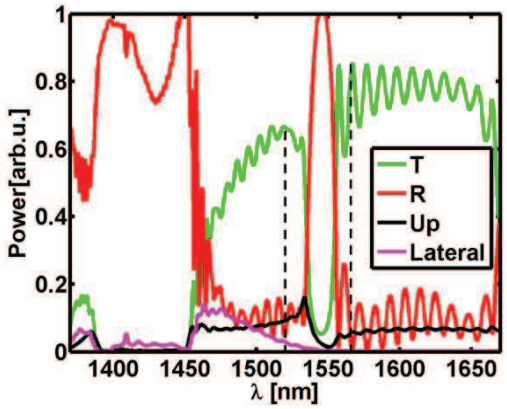


Fig. 3.7. Transmittance (T), reflectance (R), out-of-plane loss (Up) and lateral loss (Lateral) spectra, considering the value of the source waist radius $w_o$=15a/2.

Figures 3.8-3.10 show the mesoscopic self-collimation and the out-of-plane losses evaluated considering the values of the gaussian source waist radius equal to $w_0$ = 10 ×a/2, 15×a/2. In particular, the total Poynting vector has been recorded in the xy-plane and in the xz-plane and at the optimised wavelength 1567 nm, considering the

optimised source waist radius $w_o$ equal to 15a/2, and at the optimised wavelength 1587 nm, considering the source waist radius $w_o$ equal to 10a/2.

Fig. 3.8 depicts the self-normalized magnitude of the Poynting vector at the optimised wavelength 1567nm (linear scale) in xy-plane, when the optimised source waist radius is $w_o$=15a/2. The MPhC 3D wide waveguide shows a negligible reflection at the input interface (x=-15.78µm) and a collimated beam over the whole structure.

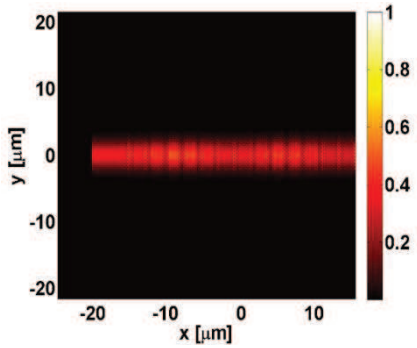


Fig. 3.8. Self-normalized magnitude of the Poynting vector at 1567nm (linear scale), considering the value of the source waist radius $w_o$=15a/2.

Fig. 3.9 shows the self-normalized magnitude of the Poynting vector at the optimised wavelength 1587nm (logarithmic scale) in xy-plane, when the source waist radius $w_o$ is decreased down to 10a/2. The MPhC 3D wide waveguide does not show a good collimation.

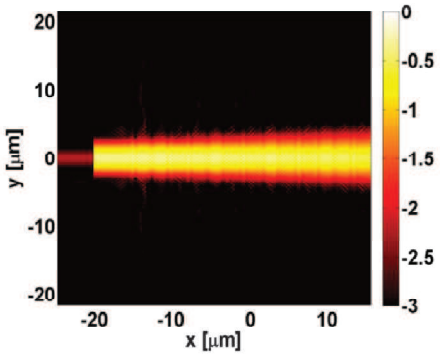


Fig. 3.9. Self-normalized magnitude of the Poynting vector at 1587nm (logarithmic scale), considering the value of the source waist radius $w_o$=10a/2.

The self-normalized magnitude of the Poynting vector at the optimised wavelength 1567nm in logarithmic scale in the xz-plane, when the optimised source waist radius is

$w_o$=15a/2, is shown in Fig. 3.10. It puts in evidence the out-of-plane losses (12%). When the source waist radius $w_o$ is equal to 10a/2, the out-of-plane loss (evaluated at the optimised wavelength 1587nm) is slightly up to about 14%.

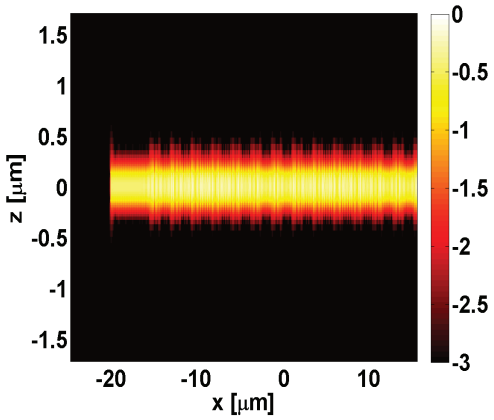


Fig. 3.10. Self-normalized magnitude of the Poynting vector at 1567nm (logarithmic scale), considering the value of the source waist radius $w_o$=15a/2.

### 3.3 *Mesoscopic Photonic Crystal 3D wide waveguide with tilted source devoted to obtain Mesoscopic Self-Collimation along tilted direction*

To obtain Mesoscopic Self-Collimation along tilted direction in a MPhC wide waveguide, it is necessary to detect a MSC point in the IFC-diagram where the IFC and the zero-curvature locus have the same tangent, as it was demonstrated in [54]. This point allows to fix the source inclination and the value of the central source wavelength with reference to the isofrequential curves (IFCs) (Fig. 3.11) of the 2D unitary cell of MPhC described in Fig. 1.13. Fig. 3.11 shows a point, where a IFC is maximally flat. To this point corresponds the pair of values of the source inclination (18.72°) and of the central source wavelength (1927 nm) that allow to obtain the mesoscopic self-collimation.

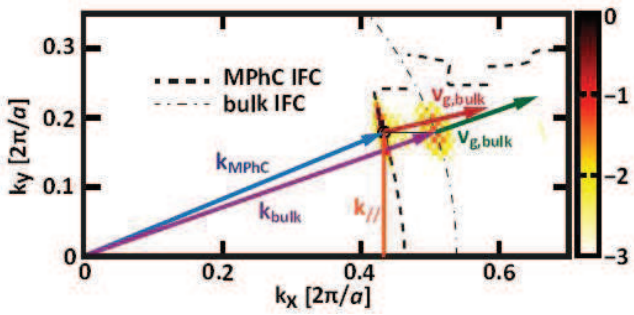


Fig. 3.11. The IFC of the 2D unitary cell of MPhC (dashed thick black curve) and the bulk IFC (dot-dashed thin black curve) are represented, calculated by means of the 2D plane wave expansion method (2D-MPB). The self-normalised absolute value of the spatially Fourier transformed *z*-component of the magnetic field (logarithmic scale) is represented. The wavevectors of the MPhC (blue arrow) and of the bulk (violet arrow), the group velocity vectors of the MPhC (dark red arrow) and of the bulk (the green arrow) are represented [54].

The MPhC 3D wide waveguide has the same geometrical and physical parameters of the structure described in Fig. 3.6 and on the left of the MPhC region the gaussian source with waist radius $w_o$=15a/2 is tilted of 18.72° compared to the x-direction, has the central wavelength equal to 1927 nm and has a band equal to $1777nm < \lambda < 2077nm$ (Fig. 3.12).

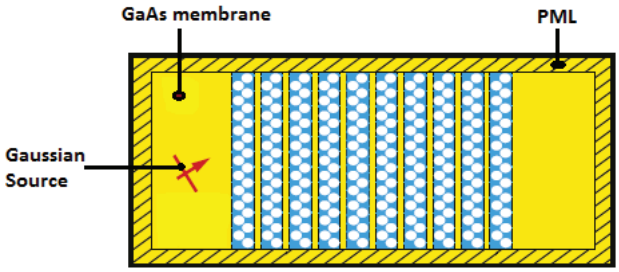


Fig. 3.12. Sketch of the mesoscopic photonic crystal 3D wide waveguide.

For this MPhC 3D wide waveguide, the transmission spectrum (normalized to the input power) has been obtained. This spectrum exhibits several peaks with almost 70 % transmission near the central source wavelength 1927 nm. However, the optimal performance is achieved for a wavelength 1954 nm with almost 77% transmission, slightly above the central source wavelength (Fig. 3.13). A mini bandgap opens around 2000 nm, corresponding to the dip appearing in Fig. 3.13, and shows a low transmission of about 20%.

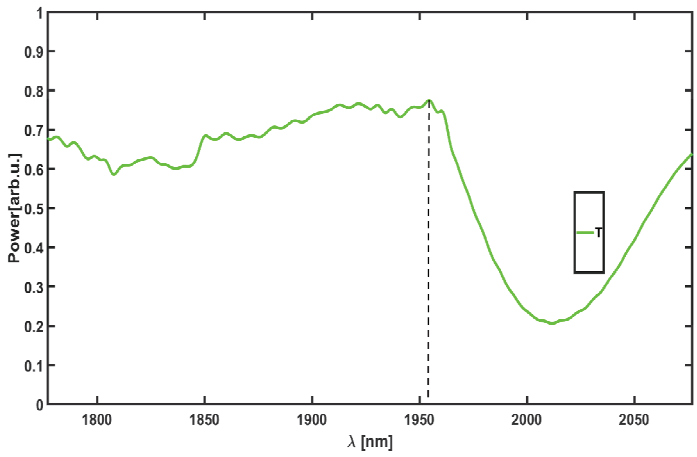


Fig. 3.13. Transmittance (T) spectrum, considering the gaussian source tilted of 18.72° compared to the x-direction and the central source wavelength equal to 1927 nm.

In order to investigate the mesoscopic self-collimation of the MPhC 3D wide waveguide, another set of 3D-FDTD simulations has been carried out. In particular, the

total Poynting vector has been recorded in the xy-plane and at the optimised wavelength 1954 nm.

Fig. 3.14 depicts the self-normalized magnitude of the Poynting vector at the optimised wavelength 1954 nm (linear scale) in xy-plane. The beam keeps the same inclination from the left of the MPhC region up to right of the MPhC region. The MPhC 3D wide waveguide shows a negligible reflection at the input PhC interface (x=-15.78μm) and a collimated beam over the whole structure.

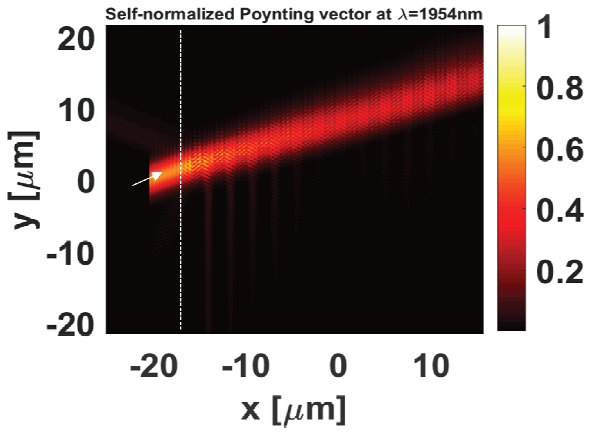


Fig. 3.14. Self-normalized magnitude of the Poynting vector at 1954 nm (linear scale), considering the gaussian source tilted of 18.72° compared to the x-direction and the central source wavelength equal to 1927 nm.

# 4. CONCLUSION

In this Ph.D. thesis I analyzed the significant properties of Mesoscopic Photonic Crystals (MPhCs) for applications as refractive index sensors, optical trapping in air and in water, and routing element.

In particular the design and the analysis of high performance MPhC 3D waveguides and cavities have been carried out by means of 3D-FDTD calculation (Lumerical).

The 3D design of the single MPhC multilayers required the analysis of the properties of the 3D unitary cells of PhCs in terms of their isofrequential curves (IFCs) obtained by means of the 3D Plane Wave Expansion Method (3D-Mit Photonic-Bands software).

Particular attention has been given to the solutions of the "single Anti-Reflection (AR) and High-Reflection (HR) MPhC multilayers geometries searching algorithm", i.e. to the triplets - the length of the PhC slab, the length of the bulk material slab, the central source normalized frequency - that satisfy both the Mesoscopic Self-Collimation (MSC) condition and the single AR or HR multilayer condition at the same time.

The considered MPhC mesoperiod is obtained by interleaving focusing slab, constituted by hole rows of a 45°-tilted hole-type square-lattice PhC, and defocusing slab, constituted by bulk material, etched on a membrane.

As example of applications in the three years of my Ph.D. program, I have designed and analysed MPhC 2D and 3D strip cavities devoted to refractive index sensor. The best result was obtained with a geometry having two 5-mesoperiod-long mesoscopic mirrors (MM), PhC slab hole radius $r = 0.28 \times a$, PhC slab overall width $d_c = 9.192 \times a$, PhC lattice constant $a$ = 360 nm, bulk slab width $d_b = 2.612 \times a$, cavity defect width $W=5.32 \times a$. The membrane has thickness equal to 270 nm and bulk refractive index $n_{GaAs}$ = 3.4, and is fully surrounded by a dielectric analyte having refractive index $n$ equal to 1, 1.3, 1.4 and 1.5. The central wavelength of the gaussian source is equal to 1550 nm. A Q-factor equal to 7888 and a sensitivity equal to 112 nm/RIU have been obtained. This structure can be exploited to tweeze-and-sense micro-

and nano-object systems thanks to the translation invariance property.

The optical trapping in air and in water has been evaluated with two approaches: the former is based on computing the optomechanical trapping potential by means of the gradient force density convolution method (Matlab) and the latter is based on the calculation of the total optomechanical force by means of Maxwell stress tensor-based method (Lumerical). The best result was obtained with a MPhC 3D wide cavity having two 5-mesoperiod-long mesoscopic mirrors (MM), PhC slab hole radius $r$ = 0.25×$a$, PhC slab overall width $d_c$ = 9.192×$a$, PhC lattice constant $a$ = 350 nm, bulk slab width $d_b$ = 2.612×$a$, cavity defect width W=5.32×$a$. The structure has thickness equal to 276 nm and bulk refractive index $n_{GaAs}$ = 3.31, is fully surrounded by air and has a width equal to 18 μm. The central wavelength of the gaussian source is equal to 1550 nm. A Q-factor equal to 3709, an optomechanical trapping potential equal to - 40 (about 4 times bigger than the minimum requirement for trapping) and a total optomechanical force equal to 2874 pN/W have been obtained.

Moreover a MPhC 3D strip cavity has been experimentally demonstrated.

I have also designed and analysed MPhC 3D strip and 3D wide waveguides, effecting the evaluation of the influence of the gaussian source waist on the collimation phenomenon. The best result was obtained with a MPhC 3D wide waveguide having 13 mesoperiods, thickness equal to 270 nm, bulk refractive index $n_{GaAs}$ = 3.4, PhC lattice constant $a$ = 360 nm, PhC hole radius $r$ = 0.28×$a$, PhC slab overall width $d_c$ = 3.536×$a$, bulk slab width $d_b$ = 3.1048×$a$. The structure is fully surrounded by air and has a width equal to 40 μm. The central wavelength of the gaussian source is equal to 1520 nm. A transmission equal to 85% and minimal unwanted reflections at PhC input interfaces, without either affecting the feasibility or the complexity of the structure, have been obtained. These results opens the way for developing a full class of routing elements that can be combined together taking advantage of the spatial and spectral reconfigurability that MSC offers. The routing elements could be obtained by interleaving different mesoperiods, that have different PhC slabs widths and different bulk slabs widths.

Finally the condition, for which the MSC along tilted direction happens in a MPhC 3D wide waveguide, has been investigated.

## BIBLIOGRAFY


[1] A. Monmayrant, F. Lozes-Dupuy, O. Gauthier-Lafaye, G. Magno, M. Grande, G. Calò, V. Petruzzelli, "*Multifunctionnal self-collimating mesoscopic photonic crystals*", In "Lasers and Electro-Optics Europe (CLEO EUROPE/IQEC), 2013 Conference on and International Quantum Electronics Conference," IEEE, pp. 1–1, 2013.

[2] V. Kivijarvi et al., "*An optical metamaterial with simultaneously suppressed optical diffraction and surface reflection*", IOP 2016.

[3] H. Kosaka et al.,"*Self-collimating phenomena in photonic crystals*", Appl. Phys Lett.**74**(9), 1212-1214 (1999).

[4] D. Chigrin, S. Enoch, C. S. Torres, G. Tayeb, "*Self-guiding in two-dimensional photonic crystals*", Optics Express, vol. 11, no. 10, pp. 1203–1211, May 2003.

[5] J. Witzens, M. Loncar, A. Scherer, "*Self-collimation in planar photonic crystals*" Selected Topics in Quantum Electronics, IEEE Journal of , vol. 8, no. 6, pp. 1246–1257, 2002.

[6] X. Shen, T. J. Cui, J. Ye, "*Anti-Reflection for Self-Collimated Beams Using Graded Index Coupler*", In "Photonics and Optoelectronics (SOPO), 2011 Symposium on," IEEE, pp. 1–4, 2011.

[7] P. T. Rakich, M. S. Dahlem, S. Tandon, M. S. Mihai Ibanescu, G. S. Petrich, J. D. Joannopoulos, L. A. Kolodziejski, E. P. Ippen, "*Achieving centimetre-scale supercollimation in a large-area two-dimensional photonic crystal*", Nature Materials, vol. 5, no. 2, pp. 93–96, 2006.

[8] Y. Chuang, T. Suleski, "*Complex rhombus lattice photonic crystals for broadband all-angle self collimation*", Journal of Optics, vol. 12, no. 3, p. 035102, 2010.

[9] R. C. Rumpf , J. J. Pazos, "*Optimization of planar self-collimating photonic crystals*", J. Opt. Soc. Am. A 30, 1297–1304 (2013).

[10] D. N. Chigrin, S. Enoch, C. M. Sotomayor-Torres, G. Tayeb, "*Self-guiding in two-dimensional photonic crystals*", in Proc. SPIE, in Symposium on Integrated Optoelectronic Devices (ISOP, 2002), pp. 63–72.

[11] X. Lin et al., "*Super-collimation with high frequency sensitivity in 2D photonic crystals induced by saddle-type van Hove singularities*", Optics Express 2013.

[12] H. Li, A. Wu, W. Li, X. Lin, C. Qiu, Z. Sheng, X. Wang, S. Zou, F. Gan, "*Millimeter-Scale and Large-Angle Self-Collimation in a Photonic Crystal Composed of Silicon Nanorods*", IEEE Photonics J. 5, 2201306 (2013).

[13] M. Noori et al., "*Highly efficient self-collimation based waveguide for Mid-IR applications*", Elsevier 2016.

[14] D.W. Prather, C. Chen, S. Shi, B. Miao, D. M. Pustai, S. Venkataraman, A. S. Sharkawy, G. J. Schneider, J. A. Murakowski, "*Ultralow-loss photonic crystal waveguides based on the self-collimation effect*", Proc. SPIE, vol. 5360, pp. 175–189, 2004.

[15] N. P. Gandji, E. Semouchkina, "*Employing Self-Collimation Phenomena in Photonic Crystals for the Invisibility Cloak Development*", IEEE, 2016.

[16] M. Liu, H. Yi, Z. Zhang, W. Lv, M. Yun, "*Mach-Zehnder interferometer in a rod-type photonic crystal*", Proc. SPIE, vol. 8847, pp. 884713–884713–5, 2013.

[17] D. Zhao, J. Zhang, P. Yao, X. Jiang, X. Chen, "*Photonic crystal Mach-Zehnder interferometer based on self-collimation*", Applied Physics Letters, vol. 90, no. 23, 231114, 2007.

[18] X. Chen, Z. Qiang, D. Zhao, Y. Wang, H. Li, Y. Qiu, W. Zhou, "*Polarization*

*beam splitter based on photonic crystal self-collimation Mach-Zehnder interferometer*", Optics Communications, vol. 284, no. 1, pp.490–493, 2011.

[19] M. M. Gupta, S. Medhekar, "*A versatile optical junction using photonic band-gap guidance and self collimation*", Applied Physics Letters, vol. 105, no. 13, 131104, 2014.

[20] C. Chen, A. Sharkawy, D. Pustai, S. Shi, D. Prather, "*Optimizing bending effciency of self-collimated beams in non-channel planar photonic crystal waveguides*", Optics Express, vol. 11, no. 23, pp. 3153–3159, Nov 2003.

[21] X. Yu, S. Fan, "*Bends and splitters for self-collimated beams in photonic crystals*", Applied Physics Letters, vol. 83, no. 16, pp. 3251–3253, 2003.

[22] A. F. Matthews, S. K. Morrison, Y. S. Kivshar, "*Self-collimation and beam splitting in low-index photonic crystals*", Optics Communications, vol. 279, no. 2, pp. 313–319, 2007.

[23] S.-G. Lee, S. S. Oh, J.-E. Kim, H. Y. Park, C.-S. Kee, "*Line-defect-induced bending and splitting of self-collimated beams in two-dimensional photonic crystals*", Applied Physics Letters, vol. 87, no. 18, 181106, 2005.

[24] Y. Zhang, Y. Zhang, B. Li, "*Optical switches and logic gates based on self-collimated beams in two-dimensional photonic crystals*", Optics Express, vol. 15, no. 15, pp. 9287–9292, Jul 2007.

[25] D. Zhao, C. Zhou, Q. Gong, X. Jiang, "*Lasing cavities and ultra-fast switch based on self-collimation of photonic crystal*", Journal of Physics D: Applied Physics, vol. 41, no. 11, p. 115108, 2008.

[26] N. Yogesh, V. Subramanian, "*Analysis of self-collimation based cavity resonator formed by photonic crystal*", Progress In Electromagnetics Research M, vol. 12, pp. 115–130, 2010.

[27] X. Chen, Z. Qiang, D. Zhao, H. Li, Y. Qiu, W. Yang, W. Zhou, "*Polarization-independent drop filters based on photonic crystal self-collimation ring resonators*", Optics Express, vol. 17, no. 22, pp. 19808–19813, Oct 2009.

[28] B. Miao, C. Chen, S. Shi, D. Prather, "*A high-efficiency in-plane splitting coupler for planar photonic Crystal self-collimation devices*", Photonics Technology Letters, IEEE, vol. 17, no. 1, pp. 61–63, Jan 2005.

[29] D. W. Prather, S. Shi, J. Murakowski, G. J. Schneider, A. Sharkawy, C. Chen, B. Miao, R. Martin, "*Self -collimation in photonic crystal structures: a new paradigm for applications and device development*", Journal of Physics D: Applied Physics, vol. 40, no. 9, p. 2635, 2007.

[30] V. Zabelin, L. A. Dunbar, N. L. Thomas, R. Houdré, M. V. Kotlyar, L. O'Faolain, T. F. Krauss, "*Self-collimating photonic crystal polarization beam splitter*", Optics Letters, vol. 32, no. 5, pp. 530–532, Mar 2007.

[31] D. Pustai, S. Shi, C. Chen, A. Sharkawy, D. Prather, "*Analysis of splitters for self-collimated beams in planar photonic crystals*", Optics Express, vol. 12, no. 9, pp. 1823–1831, May 2004.

[32] F. Qi et al., "*Experimentally simulating quantum walks with self-collimated light*", Scientific Report, 2016.

[33] T.-T. Kim, S.-G. Lee, H. Y. Park, J.-E. Kim, C.-S. Kee, "*Asymmetric Mach-Zehnder filter based on self-collimation phenomenon in two-dimensional photonic crystals*", Optics Express, vol. 18, no. 6, pp. 5384–5389, Mar 2010.

[34] H. M. Nguyen, M. A. Dundar, R. W. van der Heijden, E. W. J. M. van der Drift, H. W. M. Salemink, S. Rogge, J. Caro, "*Compact Mach-Zehnder interferometer based on self-collimation of light in a silicon photonic crystal*", Optics Express, vol. 18, no. 7, pp. 6437–6446, Mar 2010.

[35] T.-T. Kim, S.-G. Lee, S.-H. Kim, J.-E. Kim, H. Y. Park, C.-S. Kee, "*Ring-type Fabry-Pérot filter based on the self-collimation effect in a 2D photonic crystal*", Optics Express, vol. 18, no. 16, pp. 17106–17113, Aug 2010.

[36] R. C. Rumpf, J. Pazos, C. R. Garcia, L. Ochoa, R. Wicker, "*3D Printed Lattices with Spatially Variant Self-Collimation*", Progress In Electromagnetics Research, vol. 139, pp. 1–14, 2013.

[37] R. Pollès, E. Centeno, J. Arlandis, A. Moreau, "*Self-collimation and focusing effects in zero-average index metamaterials*", Optics Express, vol. 19, no. 7, pp. 6149–6154, Mar 2011.

[38] V. Mocella, S. Cabrini, A. Chang, P. Dardano, L. Moretti, I. Rendina, D. Olynick, B. Harteneck, S. Dhuey, "*Self-collimation of light over millimeter-scale distance in a quasi-zero-average-index metamaterial*", Physical Review Letters, vol. 102, no. 13, p. 133902, 2009.

[39] I. Pérez-Arjona, V. J. Sánchez-Morcillo, J. Redondo, V. Espinosa, K. Staliunas, "*Theoretical prediction of the nondiffractive propagation of sonic waves through periodic acoustic media*", Physical Review B, vol. 75, no. 1, p. 014304, 2007.

[40] E. Soliveres, V. Espinosa, I. Pérez-Arjona, V. J. Sánchez-Morcillo, K. Staliunas, "*Self collimation of ultrasound in a three-dimensional sonic crystal*", Applied Physics Letters, vol. 94, no. 16, p. 164101, 2009.

[41] A. Cicek, O. A. Kaya, B. Ulug, "*Wide-band all-angle acoustic self-collimation by rectangular sonic crystals with elliptical bases*", Journal of Physics D: Applied Physics, vol. 44, no. 20, p. 205104, 2011.

[42] S.-H. Kim, T.-T. Kim, S. Oh, J.-E. Kim, H. Park, C.-S. Kee, "*Experimental demonstration of self-collimation of spoof surface plasmons*", Physical Review B, vol. 83, p. 165109, Apr 2011.

[43] B. Stein, E. Devaux, C. Genet, T. W. Ebbesen, "*Self-collimation of surface plasmon beams*", Optics Letters, vol. 37, no. 11, pp. 1916–1918, Jun 2012.

[44] S. S. Oh, S.-G. Lee, J.-E. Kim, H. Y. Park, "*Self-collimation phenomena of surface waves in structured perfect electric conductors and metal surfaces*", Optics Express, vol. 15, no. 3, pp. 1205–1210, Feb 2007.

[45] Y. Shen, K. Chen, Y. Chen, X. Liu, J. Zi, "*Self-collimation in liquid surface waves propagating over a bottom with periodically drilled holes*", Physical Review E, vol. 71, p. 036301, Mar 2005.

[46] G. Magno, M. Grande, A. Monmayrant, F. Lozes-Dupuy, "*Controlled reflectivities in self-collimating mesoscopic photonic crystal*", Journal of the Optical Society of America B, vol. 31, no. 2, pp. 355-359, 2013.

[47] G. Magno, A. Monmayrant, M. Grande, F. Lozes-Dupuy, O. Gauthier-Lafaye, G. Calò, V. Petruzzelli, "*Stable planar mesoscopic photonic crystal cavities*", Opt. Lett., vol. 39, no. 14, pp. 4223-4226, 2014.

[48] G. Magno, A. Monmayrant, M. Grande, F. Lozes-Dupuy, O. Gauthier-Lafaye, G. Calò, V. Petruzzelli, "*Mesoscopic Self-Collimation: beyond the high symmetry constraint*", 2015/6/21, The European Conference on Lasers and Electro-Optics, Optical Society of America.

[49] O. Gauthier-Lafaye, A. Monmayrant, F. Lozes-Dupuy, M. Grande, G. Calò, V. Petruzzelli, J. Arlandis, E. Centeno, "*Tailoring reflection of self-collimating multilayer structures*", ecio conference 2012.

[50] J. Arlandis et al., "*Mesoscopic self-collimation and slow light in all-positive index layered photonic crystals*", Phys. Rev. Lett.108(3), 037401-4 (2012).

[51] G. Magno et al., "*Self-collimation in mesoscopic photonic crystals: from reflectivity management to stable planar cavities*", in Transparent Optical Networks

(ICTON), 2014 16th International Conference on, IEEE, pp.1-4, Gratz (Austria), July 6-10, 2014.

[52] G. Magno, A. Monmayrant, M. Grande, O. Gauthier-Lafaye, G. Calò, B. Dagens, V. Petruzzelli, "*Full optical confinement in 1D Mesoscopic Photonic Crystal-based microcavities: A preliminary experimental demonstration*", International Conference on Transparent Optical Networks, 2016-August, art. no. 7550433 (2016).

[53] M. Noori, M. Soroosh, H. Baghban, "*Self-Collimation in Photonic Crystals: Applications and Opportunities*", Annalen der physic, vol. 530, no. 2, pp. 1-21, 2018.

[54] G. Magno, "*Mesoscopic Self-Collimation in Photonic-Crystal Structures*", PhD thesis, Politecnico di Bari, 2015.

[55] J. Arlandis, *Étude de la mise en forme spatio-temporelle de la lumière dans les cristaux photonique set les métamatériaux* (Université Blaise Pascal U.F.R. Sciences et Technologies, 2012).

[56] G. Magno, A. Monmayrant, M. Grande, F. Lozes-Dupuy, O. Gauthier-Lafaye, G. Calò, V. Petruzzelli, "*Stable planar microcavities based on mesoscopic photonic crystals*", in Proc. SPIE, Integrated Optics: Devices, Materials, and Technologies XVIII, vol. 8988, pp. 89881G-1-89881G-10, S. Francisco (US), Feb. 1-6, 2014.

[57] P. Hsieh et al., "*Photon transport enhanced by transverse Anderson localization in disordered superlattices*", Nature Physics 11, 268–274 (2015).

[58] J. Liu, X. Zhou, Z. Qiao, J. Zhang, C. Zhang, T. Xiang, L. Shui, Y. Shi, L. Liu, "*Integrated Optical Chemical Sensor Based on an SOI Ring Resonator Using Phase-Interrogation*," *IEEE Photonics Journa*l, Volume 6, Number 5, October 2014.

[59] W. Scarcia, G. Palma, M. C. Falconi, F. de Leonardis, V. M. N. Passaro, F. Prudenzano, "*Electromagnetic modelling of fiber sensors for low-cost and high sensitivity temperature monitoring*", Sensors (Switzerland*)*, vol.15, no.12, pp. 29855-29870, 2015.

[60] M. Grande, R. Marani, F. Portincasa, G. Morea, V. Petruzzelli, A. D'Orazio, V. Marrocco, D. de Ceglia, M.A. Vincenti, "*Asymmetric plasmonic grating for optical sensing of thin layers of organic materials*", Sensors and Actuators B, vol.160, pp.1056-1062, Dec 2011.

[61] F. Bagci, B.Akaoglu, "*Enhancement of refractive index sensitivity in photonic crystal waveguide-based sensors by selective infiltration*", *Acta Physica Polonica A*, vol. 124, No.1, pp. 50-55, Apr. 2013.

[62] D. Zecca, A. Qualtieri, G. Magno, M. Grande, V. Petruzzelli, B. Prieto-Simon, A. D'Orazio, M. De Vittorio, N.H. Voelcker, T. Stomeo, "*Label-free $Si_3N_4$ photonic crystal based immunosensors for diagnostic applications*", IEEE Photonics Journal, vol. 6, No. 6, Dec. 2014.

[63] Y. Chen, T. Liu, W. Wang, Q. Zhu, W. Bi, "*Refractive index sensing performance analysis of photonic crystal Mach-Zehnder interferometer based on BP neural network optimization*", *Modern Physics Letters B*, vol. 29, No. 10, Apr. 2015.

[64] M. Grande, G. Magno, **B. Ferrara**, V. Petruzzelli, A. D'Orazio, D. Zecca, A. Qualtieri, M. De Vittorio, T. Stomeo, B. Prieto-Simon, N.H. Voelcker, "*Immunosensore in tecnologia a cristallo fotonico bidimensionale per diagnostica clinica*", in Atti del XVI Convegno Nazionale AIIC, Bari, 7-9 April 2016. Poster Presenter B.Ferrara.

[65] Grier D., "*A revolution in optical manipulation*", Nature 424, 810–816 (2003).

[66] Xie C., Goodman C., Dinno M., Li Y., "*Real-time Raman spectroscopy of optically trapped living cells and organelles*", Opt. Express 12(25), 6208–6214 (2004).

[67] Bustamante C., Bryant Z., Smith S.B., "*Ten years of tension: single-molecule DNA mechanics*", Nature 421, 423–427 (2003).

[68] Chiou P., Ohta A., Wu M., "*Massively parallel manipulation of single cells and microparticles using optical images*", Nature 436, 370–372 (2005).

[69] Huang L., Maerkl S. J., Martin O. J. E., "*Integration of plasmonic trapping in a microfluidic environment*", Opt. Express 17(8), 6018–6024 (2009).

[70] Juan M. L., Righini M., Quidant R., "*Plasmon nano-optical tweezers*", Nature Photon. 5, 349–356 (2011).

[71] G. Magno, A. Ecarnot, C. Pin, V. Yam, P. Gogol, R. Megy, B. Cluzel, B. Dagens, "*Integrated plasmonic nanotweezers for nanoparticle manipulation*", Optics Letters, vol. 41, no. 10, pp. 3679-3682, 2017.

[72] G. Magno, A. Ecarnot, C. Pin, V. Yam, P. Gogol, R. Megy, B. Cluzel, B. Dagens, "*Integrated Plasmonic Nanotweezers: Toward the Manipulation of Nanoobjects*", ICTON 2016.

[73] B.S. Schmidt, A.H.J. Yang, D. Erickson, M. Lipson, ''*Optofluidic Trapping and Transport on Solid Core Waveguides Within a Microfluidic Device*'', Opt. Express. 15(22), 14322–1433 (2007).

[74] P. Jing, J. Wu, G. W. Liu, E. G. Keeler, S. H. Pun, L. Y. Lin, "*Photonic Crystal Optical Tweezers with High Efficiency for Live Biological Samples and Viability Characterization*", Scientific Reports 6, 19924 (2016).

[75] Mandal S., Serey X., Erickson D., "*Nanomanipulation using silicon photonic*

*crystal resonators*", Nano Lett. 10, 99–104 (2010).

[76] Jing P., Wu J., Lin L.Y., "Patterned optical trapping with two-dimensional photonic crystal", ACS Photonics 1(5), 398–402 (2014).

[77] A. Ashkin, "*Acceleration and trapping of particles by radiation pressure*", Phys. Rev. Lett. 24(4), 156–159 (1970).

[78] A. Ashkin, J. M. Dziedzic, J. E. Bjorkholm, and S. Chu, "*Observation of a single-beam gradient force optical trap for dielectric particles*", Opt. Lett., vol. 11, no. 5, pp. 288–290, 1986.

[79] D. McGloin, J. P. Reid, "*Forty years of optical manipulation*", Opt. Photon. News 21(3), 20–26 (2010).

[80] V. G. Shvedov, A. S. Desyatnikov, A. V. Rode, W. Krolikowski, Y. S. Kivshar, "*Optical guiding of absorbing nanoclusters in air*", Opt. Express 17(7), 5743–5757 (2009).

[81] A.S. Desyatnikov, V.G. Shvedov, A.V. Rode, W. Krolikowski, Y.S. Kivshar, "*Photophoretic manipulation of absorbing aerosol particles with vortex beams: theory versus experiment*", Opt. Express 17(10), 8201–8211 (2009).

[82] V.G. Shvedov, A.V. Rode, Y.V. Izdebskaya, A.S. Desyatnikov, W. Krolikowski, Y.S. Kivshar, "*Giant optical manipulation*", Phys. Rev. Lett. 105(11), 118103 (2010).

[83] P. Zhang, Z. Zhang, J. Prakash, S. Huang, D. Hernandez, M. Salazar, D. N. Christodoulides, Z. Chen, "*Trapping and transporting aerosols with a single optical bottle beam generated by moiré techniques*", Opt. Lett. 36(8), 1491–1493 (2011).

[84] B.E.A. Saleh, M.C. Teich, "Fundamental of Photonics", 2nd Edition. John Wiley & Sons, Inc., 2 ed. April 2007.

[85] A. Gray, E. Abbena, S. Salamon, "*Modern differential geometry of curves and surfaces with Mathematica*", Third Edition. Chapman & Hall/CRC (Boca Raton, FL), 2006.

[86] F. Bloch, "*Uber die Quantenmechanik der Elektronen in Kristallgittern*", Zeitschrift fur Physik, vol. 52, no. 7-8, pp. 555‑600, 1929.

[87] S.G. Johnson, J.D. Joannopoulos, "*Block-iterative frequency-domain methods for Maxwell's equations in a planewave basis*", Optics Express, vol. 8, no. 3, pp. 173‑190, 2001.

[88] **B.Ferrara**, M.Grande, G.Calò, A.D'Orazio, V.Petruzzelli, G.Magno, B.Dagens, A.Monmayrant, O.Gauthier Lafaye, "*Design of mesoscopic photonic crystal microcavity based sensors devoted to optical tweezing applications*", XXI RINEM (Riunione Nazionale di Elettromagnetismo), ISBN: 978-88-907599-1-8, Parma, 12-14 September 2016. Oral Presenter B.Ferrara, 13/09/2016 Session 5, Presentation 4.

[89] **B.Ferrara**, M.Grande, G.Calò, A.D'Orazio, B.Dagens, A.Monmayrant, O.Gauthier-Lafaye, V.Petruzzelli, G.Magno, "*Optical sensor based on a mesoscopic photonic crystal microcavity*", ACP2016-Asia Communications and Photonics Conference, Wuhan (Cina), 2-5 November 2016, OSA Technical Digest (online) (Optical Society of America, 2016).

[90] A.Monmayrant, M.Grande, **B.Ferrara**, G.Calò, O.Gauthier-Lafaye, A.D'Orazio, B.Dagens, V.Petruzzelli and G.Magno, "*Full optical confinement in 1D mesoscopic photonic crystal-based microcavities: an experimental demonstration*", Optics Express, vol. 25, no. 23, pp. 28288-28294, 2017.

[91] A.Monmayrant, M.Grande, **B.Ferrara**, G.Calò, O.Gauthier-Lafaye, A.D'Orazio, B.Dagens, V.Petruzzelli, G.Magno, "*Confinement 3D dans une cavité à autocollimation mésoscopique*", "**Invited Paper**" in National Conference

Proceedings “Optique Toulouse 2018", Toulouse (France), 3-6 July 2018.

[92] A. Larrue, O. Gauthier-Lafaye, S. Bennefont, A. Arnoult, P. Dubreuil, F. Lozes-Dupuy, "*Precise Frequency Spacing in Photonic Crystal DFB Laser Arrays*", IEEE Photonics Technology Letters, vol. 20, no. 24, pp. 2120-2122, 2008.

[93] **B.Ferrara**, A.Ecarnot, A.Monmayrant, M.Grande, G.Calò, V.Petruzzelli, O.Gauthier-Lafaye, V.Yam, A.D’Orazio, B.Dagens, G.Magno, “*Optical trapping in 1D mesoscopic photonic crystal microcavities*”, International Conference “SPIE Photonics Europe 2018” – “Nanophotonics” (Conference 10672, Paper number: 10672-51), Strasbourg (France), 22-26 April 2018, SPIE Digital Library (Volume Title: Nanophotonics VII, Volume No.: 10672, 106721E). Oral Presenter B.Ferrara, 25/04/2018 Session 11, Presentation 3.

[94] A. Ecarnot, G. Magno, V. Yam, and B. Dagens, "*Ultra-efficient nanoparticle trapping by integrated plasmonic dimers*", Opt. Lett., vol. 43, pp. 455-458, 2018.

[95] **B.Ferrara**, M.Grande, G.Calò, A.D’Orazio, V.Petruzzelli, B.Dagens, A.Monmayrant, O.Gauthier-Lafaye, G.Magno, “*Design of anti-reflection Mesoscopic Photonic Crystal waveguides*”, Riunione congiunta SIEM-GTTI 2017, Udine, 21-23 June 2017.

[96] **B.Ferrara**, M.Grande, G.Calò, A.D’Orazio, V.Petruzzelli, B.Dagens, A.Monmayrant, O.Gauthier-Lafaye, G.Magno, “*Design of waveguides based on self-collimating mesoscopic photonic crystals*”, National Conference “2018 Fotonica AEIT Italian Conference on Photonics Technologies”, Lecce, 23-25 May 2018, IET Digital Library. Presenter B.Ferrara.

[97] **B.Ferrara**, M.Grande, G.Calò, A.D’Orazio, V.Petruzzelli, B.Dagens, A.Monmayrant, O.Gauthier-Lafaye, G.Magno, “*Design of mesoscopic photonic crystal waveguides*”, IET Journal of Engineering (JoE) 2018, Special Issue "Industry 4.0: the DIGITAI Transformation in the Engineering findings

(DIGITATE)" **Invited papers**, online ISSN: 2051-3305. Oral Presenter B.Ferrara, 11/12/2017 Session 2, Presentation 3, at the Conference "Poliba PhDays 2017. Industry 4.0: technologies, skills and human capital of the Polytechnic university of Bari" (11-12 December 2017, Bari- Polytechnic of Bari) organized by Polytechnic of Bari.